ORIGINAL ARTICLE



The numerical solution of the 3D Helmholtz equation with optimal accuracy on irregular domains and unfitted Cartesian meshes

A. Idesman¹ · B. Dey²

Received: 18 May 2021 / Accepted: 2 November 2021 © The Author(s), under exclusive licence to Springer-Verlag London Ltd., part of Springer Nature 2021

Abstract

Here, we extend the optimal local truncation error method (OLTEM) recently developed in our papers to the 3D time-independent Helmholtz equation on irregular domains. Trivial unfitted Cartesian meshes and simple 27-point discrete stencil equations are used for 3D irregular domains. The stencil coefficients for the new approach are assumed to be unknown and are calculated by the minimization of the local truncation error of the stencil equations. This provides the optimal order of accuracy of the proposed technique. At similar 27-point stencils, the accuracy of OLTEM is two orders higher for the Dirichlet boundary conditions and one order higher for the Neumann boundary conditions compared to that for linear finite elements. The numerical results for irregular domains also show that at the same number of degrees of freedom, OLTEM is even much more accurate than high-order (up to the fifth order) finite elements with much wider stencils. Compared to linear finite elements with similar 27-point stencils, at accuracy of 0.1% OLTEM decreases the number of degrees of freedom by a factor of greater than 1000. This leads to a huge reduction in computation time. The new approach can be equally applied to the Helmholtz and screened Poisson equations.

Keywords Helmholtz equation · Local truncation error · Irregular domains · Cartesian meshes · Optimal accuracy

1 Introduction

Many physical phenomena in acoustics, seismology, electromagnetic radiation, nondestructive testing, medical imaging and others can be modeled by the Helmholtz equation. Therefore, many researchers are working on the development of accurate numerical techniques for the solution of the Helmholtz equation that has a lot of important civil and military engineering applications. Many of these numerical techniques finally reduce to a discrete system with compact stencils; e.g., different modifications of the finite element method (e.g., see [1–23]), the isogeometric elements (e.g., see [24–26]), the spectral element method (e.g., see [27]), the finite difference method (e.g., see [28–35] and others). The goal of these linear and high-order numerical techniques is to provide reliable accurate solutions of the Helmholtz

equation at reasonable computational costs. The finite element method, the finite volume method, the isogeometric elements, the spectral elements and similar techniques represent very powerful tools for the solution of PDEs for a complex geometry. However, the generation of non-uniform meshes for a complex geometry is not simple and may lead to the decrease in accuracy of these techniques if 'bad' elements (e.g., elements with small angles) appear in the mesh. Moreover, the conventional derivation of discrete equations for these techniques (e.g., based on the Galerkin approaches) does not lead to the optimal accuracy.

There is a significant number of publications related to the numerical solution of different PDEs on irregular domains with uniform embedded meshes. For example, we can mention the following fictitious domain numerical methods that use uniform embedded meshes: the embedded finite difference method, the cut finite element method, the finite cell method, the Cartesian grid method, the immersed interface method, the virtual boundary method, the embedded boundary method, overlapping elements, etc; e.g., see [36–59] and many others. The main objective of these techniques is to simplify the mesh generation for irregular domains as well as to mitigate the effect of 'bad' elements. For example, the

Published online: 29 November 2021



A. Idesman alexander.idesman@ttu.edu

Department of Mechanical Engineering, Texas Tech University, Lubbock, TX 79409-1021, USA

Department of Mechanical Engineering, University of Utah, Salt Lake City, UT 84112, USA

techniques based of the finite element formulations (such as the cut finite element method, the finite cell method, the virtual boundary method and others) yield the p + 1 order of accuracy even with small cut cells generated by the complicated irregular boundary (e.g., see [36–38, 41, 56, 57, 60] and many others). The main advantage of the embedded boundary method developed in [42, 43, 53, 61, 62] is the use of a simple Cartesian mesh. The boundary conditions or fluxes in this technique are interpolated using the Cartesian grid points and this leads to the increase in the stencil width for the grid points located close to the boundary (however, the numerical techniques developed in [42, 43, 53, 61, 62] provide just the second order of accuracy for the global solution). An interesting high-order accurate approach is suggested in [63] for the Helmholtz equation on irregular domains that combines the method of difference potentials with compact high-order finite difference schemes on Cartesian meshes. Summarizing, the development of robust numerical techniques for the solution of PDEs on irregular domains that provide an optimal and high order of accuracy is still a challenging problem.

The numerical approach suggested in this paper for the 3D Helmholtz equation on irregular domains with unfitted Cartesian meshes is the extension of our previous numerical algorithm called the optimal local truncation error method developed for the 2D Helmholtz equation; see [64]. For the fictitious domain methods, the transition from the 2D to 3D case is a challenging problem because instead of a curve in the 2D case, the boundary becomes a surface in the 3D case. Therefore, the treatment of the boundary conditions for irregular domains with non-conforming meshes is significantly more difficult in the 3D case (sometimes the transition from the 2D to 3D case may lead to intractable algorithms). In this paper we use 3D Cartesian meshes with simple 27-point uniform and non-uniform stencils that include the Dirichlet and/or Neumann boundary conditions on complex irregular boundary as well as provide a high accuracy (much greater than that for other numerical approaches with conforming or non-conforming meshes). It is interesting to mention that the derivation of the new 3D approach for the Helmholtz equation is different from that in our paper [64] for the 2D case (see Remark 4 below) as well as different from that in our papers [65, 66] for the 3D wave, heat and Poisson equations (see Sect. 4 below).

The idea of the proposed OLTEM for the solution of PDEs is very simple. First, a Cartesian mesh is selected independent of the irregular domain under consideration. Then, stencil equations of a discrete system are assumed for all internal grid points of the Cartesian mesh located inside the irregular domain. The stencil equation for each internal grid point is a linear combination of the numerical values of the unknown function at a number of grid points included into the stencil. The stencil equations for all

internal grid points form the global discrete system of equations for OLTEM. The coefficients of the stencil equations are assumed to be unknown. These unknown coefficients are determined by the minimization of the order of the local truncation error for each stencil equation. This procedure includes a Taylor series expansion of the unknown exact solution at the grid points and its substitution into the stencil equation. As a result, we obtain the local truncation error in the form of a Taylor series. At this point, no information about partial differential equations is used. Then, the corresponding partial differential equations are applied at the grid points to exclude some partial derivatives in the expression for the local truncation error. Finally, the unknown coefficients of the stencil equation are calculated from a small local system of algebraic equations obtained by equating to zero the lowest terms in the Taylor series expansion of the local truncation error and by the minimization of the nonzero leading terms of the local truncation error with the least square method. The coefficients of the stencil equations are similarly calculated for the regular (uniform) stencils located far from the boundary and for the cut (nonuniform) stencils located close to the boundary. The nonuniform stencils (and uniform stencils that are close to the boundary) include the known boundary conditions at the selected boundary points located at the intersection of the boundary of a complex irregular domain with the horizontal, vertical and diagonal grid lines of the uniform Cartesian mesh. There are no unknowns at the boundary points. Finally, a fully discrete global system with unknowns at the internal grid points can be easily solved. The main advantages of OLTEM are a high optimal accuracy and the simplicity of the formation of a discrete system for irregular domains with unfitted Cartesian meshes. Changing the width of the stencil equations, different linear and high-order numerical techniques can be developed.

In Sect. 2.2, we consider the development of OLTEM for the 3D Helmholtz equation with zero loading term. The imposition of the Dirichlet and Neumann boundary conditions are described in Sect. 2.3. The extension of OLTEM to the 3D Helmholtz equation with nonzero loading term is presented in Sect. 2.4. Section 3 considers numerical examples and the comparison of OLTEM with conventional finite elements. For the derivation of many analytical expressions presented below, we use the computational program "Mathematica".

2 OLTEM for the 3D Helmholtz equation

In this section, we first introduce the Helmholtz equation and the local truncation error. Next, we derive OLTEM with 27-point stencils for the internal grid points located far from the boundary as well as located close to the boundary with



the Dirichlet boundary conditions in the case of zero load. Then, we consider OLTEM with 27-point stencils for the internal grid points located close to the boundary with the Neumann boundary conditions. Finally, we take into account nonzero load.

2.1 The Helmholtz equation and the local truncation error

In the paper, we show the development of OLTEM for the 3D Helmholtz equation as well as for its simple modification called the screened Poisson equation on an irregular domain Ω :

$$\nabla^2 u + a\beta^2 u = f,\tag{1}$$

where a=1 for the Helmholtz equation, a=-1 for the screened Poisson equation, β is the wave number for the Helmholtz equation, f(x, y, z) is the loading term, u(x, y, z) is the field variable. The Neumann boundary conditions $\mathbf{n} \cdot \nabla u = g_1$ on Γ^t and the Dirichlet boundary conditions $u = g_2$ on Γ^u are applied, where g_i (i = 1, 2) are the given functions, \mathbf{n} is the outward unit normal on Γ^t , and Γ^t and Γ^u denote the boundaries with the Neumann and Dirichlet boundary conditions, respectively.

According to OLTEM, we assume that after the space discretization with a rectangular Cartesian mesh, the stencil equation for Eq. (1) for each internal grid point can be written as an algebraic equation:

$$\sum_{i=1}^{L} (a\beta^2 h^2 m_i u_i^{\text{num}} + k_i u_i^{\text{num}}) = \bar{f},$$
(2)

where u_i^{num} is the numerical solution for function u at the *i*-th grid point, m_i and k_i are the unknown stencil coefficients to be determined, L is the number of the grid points included into a stencil, \bar{f} is the discretized loading term (see the next sections), h is the mesh size along the x-axis. The local numeration of internal grid points included into the stencil is used in Eq. (2). Many numerical techniques for the Helmholtz equation such as the finite difference method, the finite element method, the finite volume method, the isogeometric elements, the spectral elements, different meshless methods and others can be finally reduced to Eq. (2) with some specific coefficients m_i and k_i . To demonstrate the new technique, below we will assume 27-point stencils (L = 27) in the 3D case that correspond to the width of the stencils for the linear quadrilateral finite elements on Cartesian meshes. However, the stencils with any width can be used with the suggested approach.

Let us introduce the local truncation error used with OLTEM. The replacement of the numerical values of the function u_i^{num} at the grid points in Eq. (2) by the exact solution u_i to Eq. (1) leads to the residual of this equation called the local truncation error e of the discrete equation, Eq. (2):

$$e = \sum_{i=1}^{L} (a\beta^2 h^2 m_i u_i + k_i u_i) - \bar{f},$$
(3)

where we assume the existence of the exact solution as well as that the function u(x, y, z) is sufficiently smooth (the numerical results in Sect. 3.4 show that OLTEM can be also used with non-smooth functions). Calculating the difference between Eqs. (3) and (2) we can get

$$e = \sum_{i=1}^{L} \{a\beta^{2}h^{2}m_{i}[u_{i} - u_{i}^{\text{num}}] + k_{i}[u_{i} - u_{i}^{\text{num}}]\}$$

$$= \sum_{i=1}^{L} (a\beta^{2}h^{2}m_{i}\bar{e}_{i} + k_{i}\bar{e}_{i}),$$
(4)

where $\bar{e}_i = u_i - u_i^{\text{num}}$ are the errors of function u at the grid points i. As can be seen from Eq. (4), the local truncation error e is a linear combination of the errors of the function u at the grid points i which are included into the stencil equation.

2.2 Zero load f = 0 in Eq. (1)

Here, we present 27-point uniform stencils that will be used for the internal grid points located far from the boundary and 27-point non-uniform stencils that will be used for the grid points located close to the boundary with the Dirichlet boundary conditions. Let us consider a 3D bounded domain and a Cartesian rectangular mesh with a mesh size h where h is the size of the mesh along the x-axis, $b_y h$ and $b_z h$ are the sizes of the mesh along the y- and z-axes (b_y and b_z are the aspect ratios of the mesh); see Fig. 1. The 27-point stencil considered here is similar to that for the 3D linear quadrilateral finite elements. The spatial locations of the 26 degrees of freedom that are close to the internal degree of freedom u_{14} and contribute to the 27-point stencil for this degree of freedom are shown in Fig. 1 for the case when the boundary and the Cartesian mesh are matching or when the degree of freedom u_{14} is located far from the boundary. In the case of non-matching grids when the grid points do not coincide with the boundary, the grid points that are located outside the physical domain are moved to the boundary of the physical domain as shown in Fig. 2 and form 27-point nonuniform stencils for the internal grid points u_{14} located close to the boundary. For convenience, the local numeration of the grid points from 1 to 27 is used in Figs. 1 and 2 as well as in the derivations below for



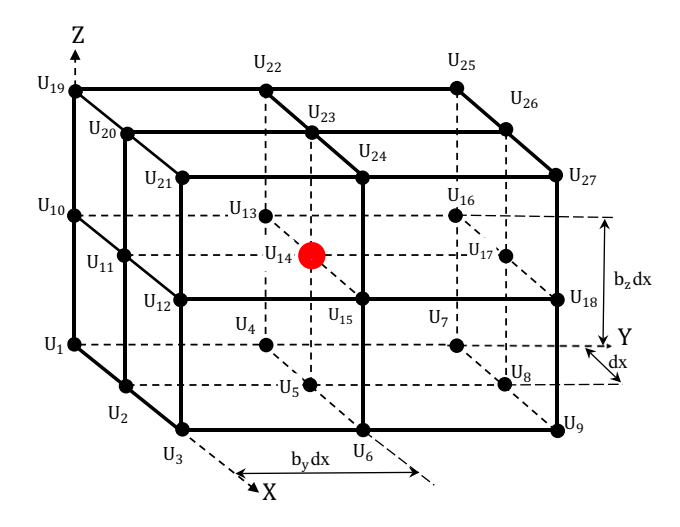


Fig. 1 The spatial locations of the degrees of freedom u_p (p = 1, 2, ..., 27) contributing to the 27-point uniform stencil for the internal degree of freedom u_{14} located far from the boundary

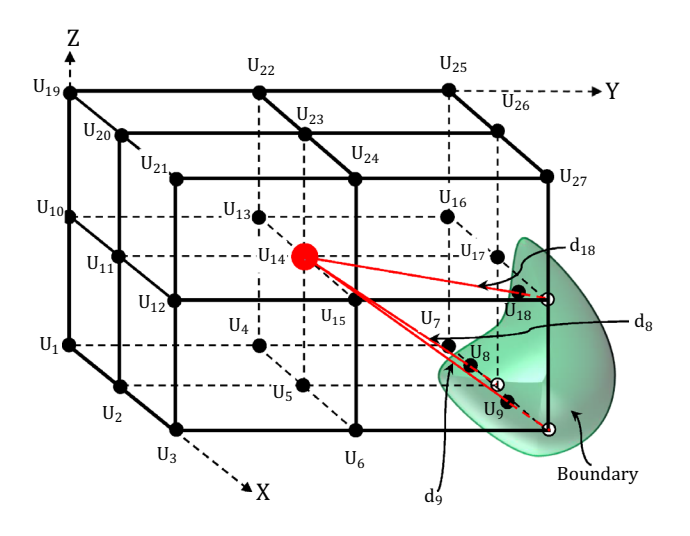
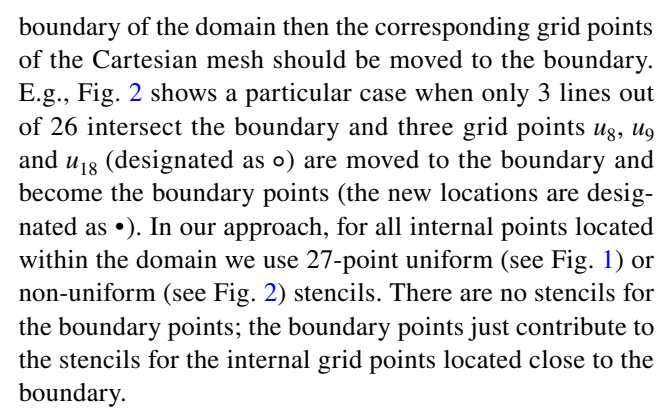


Fig. 2 The spatial locations of the degrees of freedom u_p (p = 1, 2, ..., 27) contributing to the 27-point nonuniform stencil for the internal degree of freedom u_{14} located close to the boundary

the 27-point uniform and non-uniform stencils. To find the locations of the abovementioned boundary points that are included into the stencil for the degree of freedom u_{14} (see Fig. 2) we join the central point u_{14} with the 26 closest grid points of the Cartesian mesh; i.e., we have 26 straight lines starting from point u_{14} . If any of these lines intersects the



To describe the coordinates of the boundary points for non-uniform stencils (see Fig. 2) we introduce 27 coefficients $0 \le d_p \le 1$ (p = 1, 2, ..., 27) as follows (see also Fig. 2):

$$\begin{aligned} x_p &= x_{14} + (i-2)d_p h, \quad y_p &= y_{14} + (j-2)d_p b_y h, \\ z_p &= z_{14} + (k-2)d_p b_z h, \end{aligned} \tag{5}$$

where $d_{14}=0$, p=9(k-1)+3(j-1)+i with i,j,k=1,2,3. Equation (5) can be also used for the coordinates of the grid points inside the domain with the corresponding coefficients d_p equal to unity ($d_p=1$). E.g., only three coefficients $d_8<1$, $d_9<1$ and $d_{18}<1$ in Fig. 2 are smaller than one and all other d_p coefficients are equal to unity, $d_p=1(p=1,\ldots,7,10,\ldots,13,15,\ldots,17,19,\ldots,27)$.

Equation (2) for the 27-point uniform (see Fig. 1) or nonuniform (see Fig. 2) stencil for the grid point u_{14} can be explicitly rewritten as follows:

$$a\beta^2 h^2 \sum_{p=1}^{27} m_p u_p^{\text{num}} + \sum_{p=1}^{27} k_p u_p^{\text{num}} = \bar{f}_{14}, \tag{6}$$

where the right-hand side in Eq. (6) is zero, $\bar{f}_{14} = 0$, in the case of zero load f = 0 in Eq. (1), the unknown coefficients m_p and k_p (p = 1, 2, ..., 27) are to be determined from the minimization of the local truncation error.

Remark 1 Only 53 out of the 54 coefficients m_p , k_p $(p=1,2,\ldots,27)$ in Eq. (6) can be considered as unknown coefficients. This can be explained as follows. In the case of zero load f=0 and $\bar{f}_{14}=0$, Eq. (6) can be rescaled by the division of the left- and right-hand sides of Eq. (6) by any scalar a_1 . For example, let us select $a_1=k_{14}$. In this case the rescaled coefficients \bar{m}_p , \bar{k}_p $(p=1,2,\ldots,27)$ of the stencil equation are: $\bar{m}_p=m_p/k_{14}$ $(p=1,2,\ldots,27)$, $k_{14}=1$, $\bar{k}_p=k_p/k_{14}$ $(p=1,2,\ldots,13,15,\ldots,27)$; i.e., there are only 53 unknown rescaled coefficients. The case of nonzero load $\bar{f}_{14}\neq 0$ can be similarly treated because the term \bar{f}_{14} is a linear function of the coefficients m_p and k_p (see Eq. (25) below).



Remark 2 The coefficients a and m_p in Eq. (6) can be combined into new m_p coefficients (a=1 for the Helmholtz equation and a=-1 for the screened Poisson equation). To simplify the notations, in the paper the formulas for the m_p coefficients are given for the Helmholtz equation with a=1. For the screened Poisson equation, the m_p coefficients equal to those for the Helmholtz equation with the negative sign.

For the calculation of the local truncation error, let us expand the exact solution $u_p(p=1,2,\ldots,13,15,16,\ldots,27)$ to the Helmholtz equation into a Taylor series at small $h \ll 1$ as follows (see also Eq. (5)):

$$\begin{split} u_{p} &= u_{14} + \frac{\partial u_{14}}{\partial x} [(i-2)d_{p}h] \\ &+ \frac{\partial u_{14}}{\partial y} [(j-2)d_{p}b_{y}h] + \frac{\partial u_{14}}{\partial z} [(k-2)d_{p}b_{z}h] \\ &+ \frac{\partial^{2}u_{14}}{\partial x^{2}} \frac{[(i-2)d_{p}h]^{2}}{2!} \\ &+ \frac{\partial^{2}u_{14}}{\partial y^{2}} \frac{[(j-2)d_{p}b_{y}h]^{2}}{2!} \\ &+ \frac{\partial^{2}u_{14}}{\partial z^{2}} \frac{[(k-2)d_{p}b_{z}h]^{2}}{2!} \\ &+ 2 \frac{\partial^{2}u_{14}}{\partial x \partial y} \frac{[(i-2)d_{p}h][(j-2)d_{p}b_{y}h]}{2!} \\ &+ 2 \frac{\partial^{2}u_{14}}{\partial x \partial z} \frac{[(i-2)d_{p}h][(k-2)d_{p}b_{z}h]}{2!} \\ &+ 2 \frac{\partial^{2}u_{14}}{\partial y \partial z} \frac{[(j-2)d_{p}b_{y}h][(k-2)d_{p}b_{z}h]}{2!} \\ &+ 2 \frac{\partial^{2}u_{14}}{\partial y \partial z} \frac{[(j-2)d_{p}b_{y}h][(k-2)d_{p}b_{z}h]}{2!} + \cdots, \end{split}$$

where p = 9(k-1) + 3(j-1) + i with i, j, k = 1, 2, 3; see Fig. 2. The exact solution u_{14} to Eq. (1) at $x = x_{14}$, $y = y_{14}$ and $z = z_{14}$ meets the following equations:

$$\frac{\partial^2 u_{14}}{\partial x^2} = -\frac{\partial^2 u_{14}}{\partial y^2} - \frac{\partial^2 u_{14}}{\partial z^2} - a\beta^2 u_{14},\tag{8}$$

$$\frac{\partial^{(i+j+k+2)} u_{14}}{\partial x^{i+2} \partial y^j \partial z^k} = -\frac{\partial^{(i+j+k+2)} u_{14}}{\partial x^i \partial y^{j+2} \partial z^k} - \frac{\partial^{(i+j+k+2)} u_{14}}{\partial x^i \partial y^j \partial z^{k+2}} - a\beta^2 \frac{\partial^{(i+j+k)} u_{14}}{\partial x^i \partial y^j \partial z^k}$$
(9)

with $i, j, k = 0, 1, 2, 3, 4, \dots$ Here, Eq. (9) is directly obtained by the differentiation of Eq. (8) with respect to x, y and z. Similar to Eq. (3), inserting the exact solution given by Eqs. (7)–(9) into the stencil equation, Eq. (6), instead of the numerical solution, we will get the following local truncation error in space e:

$$\begin{split} e &= b_1 u_{14} + h \left[b_2 \frac{\partial u_{14}}{\partial x} + b_3 \frac{\partial u_{14}}{\partial y} + b_4 \frac{\partial u_{14}}{\partial z} \right] \\ &+ h^2 \left[b_5 \frac{\partial^2 u_{14}}{\partial x \partial y} + b_6 \frac{\partial^2 u_{14}}{\partial x \partial z} + b_7 \frac{\partial^2 u_{14}}{\partial y^2} \right. \\ &+ b_8 \frac{\partial^2 u_{14}}{\partial y \partial z} + b_9 \frac{\partial^2 u_{14}}{\partial z^2} + b_{10} \beta^2 u_{14} \right] \\ &+ b_8 \left[b_{11} \frac{\partial^3 u_{14}}{\partial x \partial y^2} + b_{12} \frac{\partial^3 u_{14}}{\partial x \partial y \partial z} \right. \\ &+ b_{13} \frac{\partial^3 u_{14}}{\partial x \partial z^2} + b_{14} \frac{\partial^3 u_{14}}{\partial y^3} + b_{15} \frac{\partial^3 u_{14}}{\partial y^2 \partial z} + b_{16} \frac{\partial^3 u_{14}}{\partial y \partial z^2} \\ &+ b_{17} \frac{\partial^3 u_{14}}{\partial z^3} + b_{18} \beta^2 \frac{\partial u_{14}}{\partial x} \right. \\ &+ b_{19} \beta^2 \frac{\partial^4 u_{14}}{\partial y} + b_{20} \beta^2 \frac{\partial^4 u_{14}}{\partial x} \right] + h^4 \left[b_{21} \frac{\partial^4 u_{14}}{\partial x \partial y^3} \right. \\ &+ b_{22} \frac{\partial^4 u_{14}}{\partial x \partial y^2 \partial z} + b_{23} \frac{\partial^4 u_{14}}{\partial x \partial y \partial z^2} \right. \\ &+ b_{24} \frac{\partial^4 u_{14}}{\partial x \partial x^2} + b_{25} \frac{\partial^4 u_{14}}{\partial y^4} + b_{26} \frac{\partial^4 u_{14}}{\partial y^3} \\ &+ b_{27} \frac{\partial^4 u_{14}}{\partial y^2 \partial z^2} + b_{28} \frac{\partial^4 u_{14}}{\partial y \partial z^3} + b_{29} \frac{\partial^4 u_{14}}{\partial z^2} \\ &+ b_{30} \beta^2 \frac{\partial^2 u_{14}}{\partial y \partial z} + b_{31} \beta^2 \frac{\partial^2 u_{14}}{\partial x \partial y^3 \partial z} + b_{32} \beta^2 \frac{\partial^2 u_{14}}{\partial y^2} \\ &+ b_{33} \beta^2 \frac{\partial^2 u_{14}}{\partial y \partial z} + b_{34} \beta^2 \frac{\partial^2 u_{14}}{\partial z^2} + b_{35} \beta^4 u_{14} \right] \\ &+ h^5 \left[b_{36} \frac{\partial^5 u_{14}}{\partial x \partial y \partial z^3} + b_{40} \frac{\partial^5 u_{14}}{\partial x \partial y^3 \partial z} + b_{48} \frac{\partial^5 u_{14}}{\partial x \partial y^2 \partial z^3} \right. \\ &+ b_{49} \frac{\partial^5 u_{14}}{\partial y \partial z} + b_{43} \frac{\partial^5 u_{14}}{\partial y^3 \partial z^2} + b_{44} \frac{\partial^5 u_{14}}{\partial y^2 \partial z^3} \\ &+ b_{45} \frac{\partial^5 u_{14}}{\partial y \partial z} + b_{46} \frac{\partial^5 u_{14}}{\partial z^5} + b_{47} \frac{\partial^5 u_{14}}{\partial x^3 \partial y^2} \\ &+ b_{48} \beta^2 \frac{\partial^3 u_{14}}{\partial x \partial y \partial z} + b_{49} \beta^2 \frac{\partial^3 u_{14}}{\partial x \partial z^2} \\ &+ b_{50} \beta^2 \frac{\partial^3 u_{14}}{\partial x^3} + b_{51} \beta^2 \frac{\partial^3 u_{14}}{\partial y^2 \partial z} + b_{52} \beta^2 \frac{\partial^3 u_{14}}{\partial y \partial z^2} \\ &+ b_{53} \beta^2 \frac{\partial^3 u_{14}}{\partial x^3} + b_{51} \beta^2 \frac{\partial^3 u_{14}}{\partial y^3} + b_{56} \beta^4 \frac{\partial^5 u_{14}}{\partial z} \\ &+ b_{54} \beta^4 \frac{\partial^5 u_{14}}{\partial x^3} + b_{55} \beta^4 \frac{\partial^5 u_{14}}{\partial y^3} + b_{56} \beta^4 \frac{\partial^5 u_{14}}{\partial y \partial z^2} \\ &+ b_{54} \beta^4 \frac{\partial^5 u_{14}}{\partial x^3} + b_{55} \beta^4 \frac{\partial^3 u_{14}}{\partial y^3} + b_{56} \beta^4 \frac{\partial^5 u_{14}}{\partial y^3} \\ &+ b_{54} \beta^4 \frac{\partial^5 u_{14}}{$$



where the coefficients b_p (p = 1, 2, ... 165) are expressed in terms of the coefficients m_j and k_j (j = 1, 2, ..., 27); see Appendix 1. Starting from the sixth order of the local truncation error, we do not show all coefficients b_p in Eq. (10) (we show only the first and last coefficients b_p for the corresponding order). Here we should mention that the expression for the local truncation error, Eq. (10), includes the first-order derivatives with respect to x only (the higher-order derivatives with respect to x are excluded with the help of Eqs. (8)–(9)). We should also note that in Eq. (10) as well as in the equations considered below, the symbol b_p (p = 1, 2, ... 165) designates the coefficients in the expression for the local truncation error while the symbols b_y and b_z in Eq. (5) and other parts of the paper designate the aspect ratios of Cartesian meshes.

To obtain the optimal order of accuracy of the local truncation error in Eq. (10) at small $h \ll 1$, we will equate to zero the coefficients b_p in Eq. (10) for the smallest orders of h. First, let us consider the case of uniform stencils with $d_i = 1$ (i = 1, 2, ..., 27); see Fig. 1. In this case, the analytical study of coefficients b_p with the help of Mathematica shows that we can equate to zero the first 56 coefficients b_p (p = 1, 2, ..., 56) in Eq. (10). However, some of these coefficients are linearly dependent. Therefore, we will zero the following b_p coefficients:

$$b_p = 0,$$

$$p = 1, 2, \dots, 20, 22, 23, 25, 26, 27, 29, \dots, 35, 38, 42, 43, 47, \dots,$$

$$53, 65, 71, 72, 74, 75, 76, 78, 102, 106, 107, 146,$$
(11)

as well as we use the condition $k_{14} = 1$ (see the Remark 1 after Eq. (6)). The analytical solution of the algebraic equations, Eq. (11), calculated with help of Mathematica yields the following coefficients m_i and k_i (i = 1, 2, ..., 27) of the stencil equation, Eq. (6):

$$k_{1} = k_{3} = k_{7} = k_{9} = k_{19}$$

$$= k_{21} = k_{25} = k_{27} = -\frac{(5(b_{z}^{2} + 1)b_{y}^{2} + 5b_{z}^{2} + 9)}{8(125(b_{z}^{2} + 1)b_{y}^{2} + 125b_{z}^{2} + 9)},$$

$$k_{2} = k_{8} = k_{20}$$

$$= k_{26} = \frac{(5(b_{z}^{2} - 5)b_{y}^{2} - 25b_{z}^{2} + 9)}{500(b_{z}^{2} + 1)b_{y}^{2} + 500b_{z}^{2} + 36},$$

$$k_{4} = k_{6} = k_{22}$$

$$= k_{24} = \frac{(-25(b_{z}^{2} + 1)b_{y}^{2} + 5b_{z}^{2} + 9)}{500(b_{z}^{2} + 1)b_{y}^{2} + 500b_{z}^{2} + 36},$$

$$k_{10} = k_{12} = k_{16} = k_{18} = \frac{((5 - 25b_{z}^{2})b_{y}^{2} - 25b_{z}^{2} + 9)}{500(b_{z}^{2} + 1)b_{y}^{2} + 500b_{z}^{2} + 36},$$

$$k_{5} = k_{23} = \frac{(25(b_{z}^{2} - 5)b_{y}^{2} + 25b_{z}^{2} - 9)}{250(b_{z}^{2} + 1)b_{y}^{2} + 250b_{z}^{2} + 18},$$

$$k_{11} = k_{17} = \frac{(25(b_{z}^{2} + 1)b_{y}^{2} + 250b_{z}^{2} + 18},$$

$$k_{13} = k_{15} = \frac{(-25(5b_{z}^{2} - 1)b_{y}^{2} + 25b_{z}^{2} - 9)}{250(b_{z}^{2} + 1)b_{y}^{2} + 250b_{z}^{2} + 18},$$

$$k_{14} = 1, m_{1} = m_{3} = m_{7} = m_{9} = m_{19} = m_{21} = m_{25}$$

$$= m_{27} = -\frac{(7(5b_{z}^{2} + 9)b_{y}^{2} + 63b_{z}^{2} + 183)}{672(125(b_{z}^{2} + 1)b_{y}^{2} + 125b_{z}^{2} + 9)},$$

$$m_{2} = m_{8} = m_{20} = m_{26} = -\frac{(7(25b_{z}^{2} - 9)b_{y}^{2} - 63b_{z}^{2} + 183)}{336(125(b_{z}^{2} + 1)b_{y}^{2} + 125b_{z}^{2} + 9)},$$

$$m_{10} = m_{12} = m_{16} = m_{18} = \frac{(-35(5b_{z}^{2} + 9)b_{y}^{2} + 63b_{z}^{2} + 183)}{336(125(b_{z}^{2} + 1)b_{y}^{2} + 125b_{z}^{2} + 9)},$$

$$m_{5} = m_{23} = \frac{(-35(25b_{z}^{2} - 9)b_{y}^{2} - 63b_{z}^{2} + 195)}{168(125(b_{z}^{2} + 1)b_{y}^{2} + 125b_{z}^{2} + 9)},$$

$$m_{11} = m_{17} = \frac{(-7(125b_{z}^{2} + 9)b_{y}^{2} + 315b_{z}^{2} + 195)}{168(125(b_{z}^{2} + 1)b_{y}^{2} + 125b_{z}^{2} + 9)},$$

$$m_{13} = m_{15} = \frac{(-35(25b_{z}^{2} - 9)b_{y}^{2} + 315b_{z}^{2} - 183)}{168(125(b_{z}^{2} + 1)b_{y}^{2} + 125b_{z}^{2} + 9)},$$

$$m_{14} = -\frac{5(7(125b_{z}^{2} + 9)b_{y}^{2} + 63b_{z}^{2} + 39)}{84(125(b_{z}^{2} + 1)b_{y}^{2} + 125b_{z}^{2} + 9)}.$$



Inserting these coefficients m_i and k_i (i = 1, 2, 3, ..., 27) from Eq. (12) into Eq. (10), we will get the following local truncation error in space e for uniform stencils:

$$e = \frac{3b_y^2 b_z^2 h^6 ((b_y^4 - 1) \frac{\partial^6 u_{14}}{\partial y^6} + (b_z^4 - 1) \frac{\partial^6 u_{14}}{\partial z^6} - \beta^6 u_{14})}{8(125b_y^2 (b_z^2 + 1) + 125b_z^2 + 9)} + O(h^8),$$
(13)

i.e., the coefficients m_i and k_i (i = 1, 2, ..., 27) given by Eq. (12) zero all coefficients b_p (p = 1, 2, ..., 56) in Eq. (10) up to the fifth order and provide the global fourth order of accuracy of OLTEM on regular domains.

Remark 3 It is interesting to mention that 9-point stencils in the 2D case and 27-point stencils in the 3D case can provide the global sixth order of accuracy for the Helmholtz equation on regular domains; e.g., see [67, 68]. The optimal global fourth order of accuracy of OLTEM with the 27-point stencils on regular domains is explained by the form of the stencil equations, Eq. (6). For example, we can also get the global sixth order of accuracy for OLTEM with 27-point stencils on regular domains if we assume that the stencil coefficients m_p and k_p in Eq. (6) are polynomial functions of the mesh size h (e.g., see our paper [69] for the time-dependent wave equation in the 2D case). However, in the case of irregular domains, we can get the global fourth order of accuracy for OLTEM and we use the simple 27-point stencils given by Eq. (6) to simplify the derivations.

Next, let us consider non-uniform stencils; see Fig. 2. If we equate to zero the first 35 coefficients $b_n = 0$ (p = 1, 2, ..., 15) in Eq. (10), then, at least, we could obtain the fifth order of the local truncation error. However, for a rectangular mesh with $b_y \neq 1$ or/and $b_z \neq 1$, the corresponding system of 35 algebraic equations for some particular cases (e.g., when one point of the 27-point regular stencil lies outside the physical domain and we have a non-uniform stencil with $d_1 \neq 1$, see Fig. 2) can be analytically solved with the help of Mathematica. These solutions show that all coefficients k_i in this stencil equation are zeros; i.e., these solutions are inappropriate. Therefore, the maximum possible order of the local truncation error for a non-uniform stencil, Eq. (6), on a rectangular mesh corresponds to the fourth order (this can be obtained by equating to zero the first 20 coefficients $b_p = 0$ $(p = 1, 2, \dots, 20)$ in Eq. (10)).

To zero the coefficients b_p (p = 1, 2, ..., 20) for rectangular meshes and minimize the values of the coefficients b_p (p = 21, 22, ..., 165) for the fourth, fifth, sixth, seventh and eighth orders of the local truncation error for all non-uniform stencils, we use the following procedure. First, let us zero the following coefficients b_p :

$$b_p = 0, \quad p = 1, 2, \dots, 20.$$
 (14)

Then, for the coefficients b_p related to the fourth, fifth, sixth, seventh and eighth orders of the local truncation error, we use the least square method with the following residual R:

$$R = \sum_{p=21}^{35} b_p^2 + h_1 \sum_{p=36}^{56} b_p^2 + h_2 \sum_{p=57}^{84} b_p^2 + h_3 \sum_{p=85}^{120} b_p^2 + h_4 \sum_{p=121}^{165} b_p^2,$$
 (15)

where h_1 , h_2 , h_3 and h_4 are the weighting factors to be selected (e.g., the numerical experiments show that $h_1 = h_2 = h_3 = h_4 = h$ yields accurate results). The inclusion of the terms up to the eighth order is explained by the fact that for uniform meshes, the inclusion of these terms provides a sufficient number of equations for the calculation of the coefficients m_i and k_i (i = 1, 2, ..., 27); see Eq. (11).

Remark 4 It is interesting to mention that OLTEM for the 2D Helmholtz equation in our paper [64] does not include the coefficients b_p related to the seventh and eighth orders of the local truncation error.

To minimize the residual R with the constraints given by Eq. (14), we can form a new residual \bar{R} with the Lagrange multipliers λ_n :

$$\bar{R} = \sum_{p=21}^{35} b_p^2 + h_1 \sum_{p=36}^{56} b_p^2 + h_2 \sum_{p=57}^{84} b_p^2 + h_3 \sum_{p=85}^{120} b_p^2 + h_4 \sum_{p=121}^{165} b_p^2 + \sum_{p=1}^{20} \lambda_p b_p.$$
(16)

The residual \bar{R} is a quadratic function of coefficients m_i and k_i ($i=1,2,\ldots,27$) and a linear function of the Lagrange multipliers λ_p ; i.e., $\bar{R}=\bar{R}(m_i,k_i,\lambda_p)$. To minimize the residual $\bar{R}(m_i,k_i,\lambda_p)$, the following equations based on the least square method for the residual \bar{R} can be written down:

$$\frac{\partial \bar{R}}{\partial m_i} = 0, \quad \frac{\partial \bar{R}}{\partial k_i} = 0, \quad i = 1, 2, \dots, 27,$$
 (17)

$$\frac{\partial \bar{R}}{\partial \lambda_p} = 0, \quad p = 1, 2, \dots, 20, \tag{18}$$

where equation $\frac{\partial \bar{R}}{\partial k_{14}} = 0$ should be replaced by $k_{14} = 1$ (because for the stencil equation, Eq. (6), one of the coefficients m_i and k_i (i = 1, 2, ..., 27) can be arbitrary selected; e.g., $k_{14} = 1$; see Remark 1 after Eq. (6)). Equations (17) and (18) form a system of 74 linear algebraic equations with respect to 54 unknown stencil coefficients m_i and k_i (i = 1, 2, ..., 27) and 20 Lagrange multipliers λ_p (p = 1, 2, ..., 20). Solving these linear algebraic equations numerically, we can find the coefficients m_i , k_i (i = 1, 2, ..., 27) for the 27-point non-uniform stencils.



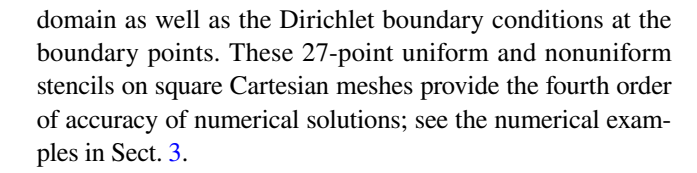
Remark 5 To estimate the computation costs of the formation and solution of 74 linear algebraic equations formed by Eqs. (17) and (18) we solved 10^6 such systems with a general MATLAB solver on a desktop computer (Processor: Intel (R) Core(TN) i9-9900 CPU @3.10 Hz 3.10 HZ). The computation 'wall' time was T = 356.76 s for 10^6 systems or the average time for one system was 0.00035676 s. Because the coefficients m_i and k_i (i = 1, 2, ..., 27) are independently calculated for different non-uniform stencils, the computation time of their calculation for different grid points can be significantly reduced on modern parallel computers. This means that for large global systems of equations, the computation time for the calculation of the coefficients m_i and k_i (i = 1, 2, ..., 27) is very small compared to that for the solution of the global system of equations. For example, for a relatively small 3D system with 216,595 degrees of freedom, the preparation and solution of the local systems took $t_1 = 3.06$ s while the solution of the global discrete system took $t_o = 66.84$ s. With mesh refinement, the number of the local systems for the stencils close to the boundary is proportional to $1/h^2$ while the number of degrees of freedom for the global system is proportional to $1/h^3$; i.e., t_a/t_l will grow with mesh refinement.

OLTEM provides the fourth (with rectangular Cartesian meshes) or the fifth (with cubic $b_y = b_z = 1$ Cartesian meshes) order of the local truncation error for the nonuniform stencils and the sixth order of the local truncation error for the uniform stencils (see Eq. (13)). For the conventional linear finite elements on uniform square meshes, the values of the coefficients m_i and k_i (i = 1, 2, ..., 27) (e.g., see [70] for the coefficients m_i and k_i used with the finite elements) provide the fourth order of the local truncation error; i.e., OLTEM improves the local truncation error in space by two orders compared to that for the conventional linear elements on uniform square meshes. These orders of accuracy are independent of the wave number β .

2.3 Boundary conditions

2.3.1 Dirichlet boundary conditions

The application of the Dirichlet boundary conditions in OLTEM is trivial and similar to that for the finite elements. We simply equate the boundary degrees of freedom of the uniform and non-uniform stencils (see Figs. 1 and 2) to the values of a given function $g_2(x, y, z)$ at the corresponding boundary points; i.e., the Dirichlet boundary conditions are exactly imposed. Here, $g_2(x, y, z)$ describes the Dirichlet boundary conditions. The final global discrete system of equations includes the 27-point uniform and nonuniform stencil equations (see Figs. 1 and 2) for all internal grid points that are located inside the



Remark 6 As shown in [62], the boundary stencils may have the local truncation error that is one order lower compared to that for internal stencils (this does not worsen the order of accuracy of the global solution).

Remark 7 The proposed technique yields accurate results for the non-uniform stencils even with very small coefficients $d_i \ll 1$. However, the new technique allows also to exclude very small coefficients $d_i \ll 1$ from calculations. For example, if $d_i \ll tol$ for some internal grid point (see Fig. 2) where tol is a small tolerance (e.g., tol = 10^{-3}), then the nonuniform stencil for this internal grid point can be removed from the global system of equations and this point can be moved to the boundary and treated as the boundary point for other stencils. In this case, the corresponding coefficients d_i for this point in other stencils can be slightly greater than one. According to the derivations in the previous section, all equations will be valid also for $d_i > 1$. The numerical experiments with a small tolerance tol = 10^{-3} show that if the point with very small coefficients $d_i \ll 1$ is moved to the boundary then the coefficients d_i for this point in other stencils can be taken as $d_i = 1$ without introducing any significant errors.

2.3.2 Neumann boundary conditions

The imposition of the Neumann boundary conditions for OLTEM is different from that for the Dirichlet boundary conditions. Our goal is to use the same 27-point uniform and non-uniform stencils equations as those in Figs. 1 and 2 because this significantly simplifies the implementation of OLTEM with unfitted Cartesian meshes. We suggest the following 27-point stencil equations for the Neumann boundary conditions:

$$a\beta^{2}h^{2} \sum_{p=1}^{27} m_{p} u_{p}^{\text{num}} + \sum_{p=1}^{27} k_{p} u_{p}^{\text{num}}$$

$$= \left[a\beta^{2}h^{3} \sum_{p=1}^{27} \bar{m}_{p} g_{1}(x_{p}, y_{p}, z_{p}) + h \sum_{p=1}^{27} \bar{k}_{p} g_{1}(x_{p}, y_{p}, z_{p}) \right] + \bar{f}_{14},$$
(19)

where $\bar{f}_{14} = 0$ in the case of zero load f = 0 in Eq. (1), the expression in the square brackets in the right-hand side of Eq. (19) is known and represents the Neumann boundary conditions at the boundary points with the coordinates x_p, y_p, z_p that are located on the boundary with the Neumann



boundary conditions (see Fig. 2), the unknown stencil coefficients m_p , \bar{m}_p , k_p , and \bar{k}_p ($p=1,2,\ldots,27$) are to be determined from the minimization of the local truncation error, the coefficients $m_p=0$ and $k_p=0$ if the stencil point with the coordinates x_p, y_p, z_p is located on the boundary with the Neumann boundary conditions; otherwise, $\bar{m}_p=0$ and $\bar{k}_p=0$ (this means that Eq. (19) includes only 54 non-zero coefficients m_p , \bar{m}_p , k_p , and \bar{k}_p), the central grid point with the coordinates x_{14} , y_{14} and z_{14} is always the internal grid point (therefore, $\bar{m}_{14}=\bar{k}_{14}=0$). Only 53 out of the 54 nonzero coefficients m_p , \bar{m}_p , k_p , and \bar{k}_p ($p=1,2,\ldots,9$) in Eq. (19) can be considered as unknown coefficients. This can be explained similar to Remark 1 after Eq. (6).

The local truncation error e of the stencil equation, Eq. (19), can be written down by the replacement of the numerical solution in Eq. (19) by the exact solution as follows:

$$e = a\beta^{2}h^{2} \sum_{p=1}^{27} m_{p}u_{p} + \sum_{p=1}^{27} k_{p}u_{p}$$

$$- a\beta^{2}h^{3} \sum_{p=1}^{27} \bar{m}_{p} \left(n_{1,p} \frac{\partial u_{p}}{\partial x} + n_{2,p} \frac{\partial u_{p}}{\partial y} + n_{3,p} \frac{\partial u_{p}}{\partial z} \right)$$

$$- h \sum_{p=1}^{27} \bar{k}_{p} \left(n_{1,p} \frac{\partial u_{p}}{\partial x} + n_{2,p} \frac{\partial u_{p}}{\partial y} + n_{3,p} \frac{\partial u_{p}}{\partial z} \right) - \bar{f}_{14},$$
(20)

where $n_{1,p}$, $n_{2,p}$ and $n_{3,p}$ (p = 1, 2, ..., 27) are the x-, y- and z-components of the outward unit normal vector \mathbf{n}_p at the boundary point p (see Fig. 2), function u(x, y, z) in Eq. (20) corresponds to the exact solution, the Neumann boundary conditions in the right-hand side of Eq. (19) are expressed in terms of the function u(x, y, z) and are moved to the left-hand side.

The rest of derivations will be similar to those in Sect. 2.2. Inserting Eqs. (7)–(9) into Eq. (20), we will get the local truncation error in space e that can be also expressed by Eq. (10) with the coefficients b_p (p = 1, 2, ..., 165) given in Appendix 2. In contrast to Sect. 2.2, now the coefficients b_p (p = 1, 2, ..., 165) depend not only on m_i , k_i and d_i but also on \bar{m}_i , \bar{k}_i , $n_{1,i}$, $n_{2,i}$ and $n_{3,i}$ (i = 1, 2, ..., 27); see Appendix 2. For the calculations of the coefficients m_i , \bar{m}_i , k_i , \bar{k}_i (i = 1, 2, ..., 27) for the uniform and non-uniform stencils, we will use the least square method with Eqs. (14)–(18). However, Eq. (17) should be modified as follows:

$$\frac{\partial \bar{R}}{\partial m_i} = 0, \quad \frac{\partial \bar{R}}{\partial \bar{m}_i} = 0, \quad \frac{\partial \bar{R}}{\partial k_i} = 0, \quad \frac{\partial \bar{R}}{\partial \bar{k}_i} = 0, \quad i = 1, 2, \dots, 27,$$
(21)

where the partial derivatives of \bar{R} in Eq. (21) are considered with respect to only non-zero coefficients m_i , \bar{m}_i , k_i , \bar{k}_i with $i=1,2,\ldots,27$ (see also the explanations for zero and non-zero coefficients after Eq. (19)); i.e., Eq. (21) as well as Eq. (17) provides 54 algebraic equations (similar to Eq. (17), equation $\frac{\partial \bar{R}}{\partial k_{14}} = 0$ should be replaced by $k_{14} = 1$). Finally,

solving 74 linear algebraic equations (Eqs. (18) and (21)) numerically, we can find the coefficients m_i , \bar{m}_i , k_i , \bar{k}_i ($i=1,2,\ldots,27$) for the 27-point uniform and non-uniform stencils. Numerical experiments show that for the Neumann boundary conditions, the coefficients $h_1 = h_2 = h_3 = h_4 = 1$ in Eq. (15) provide accurate results.

Remark 8 In contrast to Sect. 2.2, the non-uniform stencils with the Neumann boundary conditions provide the fourth-order of the local truncation error on cubic $(b_y = b_z = 1)$ meshes (the same as on rectangular meshes). This corresponds to the third order of accuracy of the numerical results for OLTEM with the Neumann boundary conditions; see the numerical examples in Sect. 3.

Remark 9 As can be seen from Eq. (19), the Neumann boundary conditions at the selected boundary points contribute to the right-hand side of the stencil equations. Similarly, the known Dirichlet boundary conditions at the selected boundary points (see the previous section) can be moved to the right-hand side of the stencil equations. This means that there are no unknowns at the boundary points for the proposed approach and the unknowns are calculated at all internal grid points. The actual number of the internal Cartesian grid points with the unknowns u_p^{num} (the stencil width) included into the stencil equations with the boundary points is smaller than 27.

2.4 Nonzero load $f \neq 0$ in Eq. (1)

The inclusion of non-zero loading term f in the partial differential equation, Eq. (1), leads to the non-zero term \bar{f}_{14} in the stencil equations, Eqs. (6) and (19) (similar to Eq. (2)). The expression for the term \bar{f}_{14} can be calculated from the procedure used for the derivation of the local truncation error in the case of zero loading function.

In the case of non-zero loading function $(f(x) \neq 0)$, Eqs. (8) and (9) for the exact solution at $x = x_{14}$, $y = y_{14}$ and $z = z_{14}$ can be modified as follows:

$$\frac{\partial^2 u_{14}}{\partial x^2} = -\frac{\partial^2 u_{14}}{\partial y^2} - \frac{\partial^2 u_{14}}{\partial z^2} - a\beta^2 u_{14} + f(x_{14}, y_{14}, z_{14}), \quad (22)$$

$$\frac{\partial^{(i+j+k+2)} u_{14}}{\partial x^{i+2} \partial y^{j} \partial z^{k}} = -\frac{\partial^{(i+j+k+2)} u_{14}}{\partial x^{i} \partial y^{j+2} \partial z^{k}}
-\frac{\partial^{(i+j+k+2)} u_{14}}{\partial x^{i} \partial y^{j} \partial z^{k+2}} - a\beta^{2} \frac{\partial^{(i+j+k)} u_{14}}{\partial x^{i} \partial y^{j} \partial z^{k}}
+\frac{\partial^{(i+j+k)} f(x_{14}, y_{14}, z_{14})}{\partial x^{i} \partial y^{j} \partial z^{k}}$$
(23)



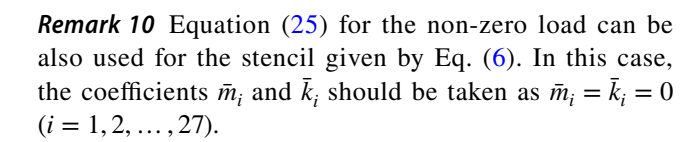
with $i, j, k = 0, 1, 2, 3, 4, \dots$ Then, inserting Eqs. (7), (22) and (23) with the exact solution to Eq. (1) into the stencil equation, Eq. (19), with non-zero \bar{f}_5 we will get the following local truncation error in space e_f :

$$\begin{split} e_f &= e - \left[\bar{f}_{14} - \left\{ \frac{h^2 f_{14}}{2} (k_1 d_1^2 - 2 \bar{k}_1 n_{1,1} d_1 + d_{10}^2 k_{10} \right. \right. \\ &+ d_{12}^2 k_{12} + d_{13}^2 k_{13} + d_{15}^2 k_{15} + d_{16}^2 k_{16} + d_{18}^2 k_{18} \\ &+ d_{19}^2 k_{19} + d_{21}^2 k_{21} + d_{22}^2 k_{22} \\ &+ d_{24}^2 k_{24} + d_{25}^2 k_{25} + d_{27}^2 k_{27} + d_3^2 k_3 + d_4^2 k_4 + d_6^2 k_6 \\ &+ d_7^2 k_7 + d_9^2 k_9 - 2 d_{10} \bar{k}_{10} n_{1,10} + 2 d_{12} \bar{k}_{12} n_{1,12} \\ &- 2 d_{13} \bar{k}_{13} n_{1,13} + 2 d_{15} \bar{k}_{15} n_{1,15} \\ &- 2 d_{16} \bar{k}_{16} n_{1,16} + 2 d_{18} \bar{k}_{18} n_{1,18} - 2 d_{19} \bar{k}_{19} n_{1,19} \\ &+ 2 d_{21} \bar{k}_{21} n_{1,21} - 2 d_{22} \bar{k}_{22} n_{1,22} \\ &+ 2 d_{24} \bar{k}_{24} n_{1,24} - 2 d_{25} \bar{k}_{25} n_{1,25} \\ &+ 2 d_{27} \bar{k}_{27} n_{1,27} + 2 d_3 \bar{k}_3 n_{1,3} - 2 d_4 \bar{k}_4 n_{1,4} \\ &+ 2 d_6 \bar{k}_6 n_{1,6} - 2 d_7 \bar{k}_7 n_{1,7} \\ &+ 2 d_9 \bar{k}_9 n_{1,9}) + h^3 (\cdots) + \cdots \right\} \bigg], \end{split}$$

where e is the local truncation error in space given by Eq. (10), f_{14} designates function f(x, y, z) calculated at $x = x_{14}$, $y = y_{14}$ and $z = z_{14}$. Equating to zero the expression in the square brackets in the right-hand side of Eq. (24), we will get the expression for \bar{f}_{14} :

$$\begin{split} \bar{f}_{14} &= \frac{h^2 f_{14}}{2} (k_1 d_1^2 - 2\bar{k}_1 n_{1,1} d_1 \\ &+ d_{10}^2 k_{10} + d_{12}^2 k_{12} + d_{13}^2 k_{13} + d_{15}^2 k_{15} + d_{16}^2 k_{16} \\ &+ d_{18}^2 k_{18} + d_{19}^2 k_{19} + d_{21}^2 k_{21} + d_{22}^2 k_{22} + d_{24}^2 k_{24} \\ &+ d_{25}^2 k_{25} + d_{27}^2 k_{27} + d_3^2 k_3 + d_4^2 k_4 + d_6^2 k_6 + d_7^2 k_7 \\ &+ d_9^2 k_9 - 2 d_{10} \bar{k}_{10} n_{1,10} + 2 d_{12} \bar{k}_{12} n_{1,12} \\ &- 2 d_{13} \bar{k}_{13} n_{1,13} + 2 d_{15} \bar{k}_{15} n_{1,15} \\ &- 2 d_{16} \bar{k}_{16} n_{1,16} + 2 d_{18} \bar{k}_{18} n_{1,18} - 2 d_{19} \bar{k}_{19} n_{1,19} \\ &+ 2 d_{21} \bar{k}_{21} n_{1,21} - 2 d_{22} \bar{k}_{22} n_{1,22} \\ &+ 2 d_{24} \bar{k}_{24} n_{1,24} - 2 d_{25} \bar{k}_{25} n_{1,25} \\ &+ 2 d_{27} \bar{k}_{27} n_{1,27} + 2 d_3 \bar{k}_3 n_{1,3} - 2 d_4 \bar{k}_4 n_{1,4} \\ &+ 2 d_6 \bar{k}_6 n_{1,6} - 2 d_7 \bar{k}_7 n_{1,7} + 2 d_9 \bar{k}_9 n_{1,9}) + h^3 (\cdots) + \cdots \end{split}$$

as well as we will get the same local truncation errors $e_f = e$ for zero and non-zero loading functions; see the attached files "RHS-Helm.pdf" and "RHS-Helm.nb" for the detailed expression of \bar{f}_{14} . This means that the coefficients m_i and k_i of the stencil equations are first calculated for zero load f=0 as described in Sects. 2.2 and 2.3. Then, the nonzero loading term \bar{f}_{14} given by Eq. (25) is used in the stencil equation, Eqs. (6) and (19).



3 Numerical examples

In this section, the computational efficiency of OLTEM developed for the 3D Helmholtz and screened Poisson equations will be demonstrated and compared with conventional FEM. OLTEM is implemented as a Matlab code. The commercial finite element software 'COMSOL' is used for the finite element simulations. Similar to FEM terminology, a grid point of a Cartesian mesh will be called a node. To compare the accuracy of the numerical results obtained by OLTEM and by FEM, the relative error e_j at the jth node and the maximum relative error e^{\max} for the function u are defined as:

$$e_{j} = \frac{\mid u_{j}^{\text{num}} - u_{j}^{\text{exact}} \mid}{u_{\text{max}}^{\text{exact}}}, \quad e^{\text{max}} = \max_{j} e_{j}, \qquad j = 1, 2, \dots, N.$$
 (26)

In Eq. (26) the superscripts 'num' and 'exact' correspond to the numerical and exact solutions, N is the total number of nodes used in calculations, $u_{\text{max}}^{\text{exact}}$ is the maximum absolute value of the exact solution for the function u over the entire domain. We also use the relative error $||e||_2$ in the L^2 norm for finite elements (e.g., see [71]) and the relative error $||e||_2$ in the l^2 norm (e.g., see [72]) for OLTEM:

$$\|e\|_2 = \frac{\|u^{\text{exact}} - u^{\text{num}}\|_2}{\|u^{\text{exact}}\|_2},$$
 (27)

where $\|u^{\text{exact}} - u^{\text{num}}\|_2 = \{\operatorname{dx}\operatorname{dy}\operatorname{dz}\sum_{j=0}^{N_z}\sum_{j=0}^{N_z}\sum_{k=0}^{N_z}a_{i,j,k}[u^{\text{exact}}(x_i,y_j,z_k) - u^{\text{num}}(x_i,y_j,z_k)]^2\}^{\frac{1}{2}}$; N_x , N_y and N_z are the numbers of Cartesian grid points along x-, y- and z-axes, x_i , y_j and z_k are the coordinates of Cartesian grid points; for the grid point with the coordinates x_i , y_j , z_k , the coefficient $a_{i,j,k} = 1$ if the grid point is located inside the domain and $a_{i,i,k} = 0$ otherwise.

The efficiency of conventional FEM and OLTEM is compared by the solution of two test problems with the following smooth exact solutions to the Helmholtz equation (Eq. (2) with a = 1):

$$u(x, y, z) = \cos(2\pi x)\cos(2\pi y)\cos(2\pi z) \tag{28}$$

with $\beta^2 = 12\pi^2$ and zero loading function f = 0; and

$$u(x, y, z) = \sin(5\pi x)\cos[\pi(3y + 2z)]$$
 (29)

with $\beta^2 = 100$ and non-zero loading function $f(x, y, z) = (100 - 38\pi^2) \sin(5\pi x) \cos[\pi(3y + 2z)]$ (see Sects. 3.1–3.3) as well as a test problem with a non-smooth



solution (see Sect. 3.4). For the screened Poisson equation (Eq. (2) with a = -1), we consider another test problem with the following exact solution:

$$u(x, y, z) = \cos[\pi(2x + 3y)]e^{4\pi(z-1)}$$
(30)

with $\beta^2 = 3\pi^2$ and zero loading function f = 0 (see Sect. 3.5).

First, in Sect. 3.1 we solve the Helmholtz equation with nonzero loading on a regular cubic domain and the exact solution given by Eq. (29). Then, we consider an irregular domain represented by a prism ABCDOPQR with a spherical hole; see Fig. 5a. Figure 5b shows the Cartesian mesh used for OLTEM. For convenience, Cartesian meshes for the prism are generated in such a way that three grid planes of the Cartesian mesh are always matched with the faces APOD, ABQP and ABCD; depending on the mesh size h grid planes can be matched or non-matched with the faces BCRQ and CDOR; and the inclined face OPQR and the spherical surface of the hole are always non-matched with the Cartesian grid planes. An example of a typical tetrahedral mesh for the prism generated by COMSOL for the conventional FEM is shown in Fig. 5c, d. In Sect. 3.2, we solve the Helmholtz equation for the 3D prism with the Dirichlet boundary conditions imposed along the entire boundary. In Sect. 3.3, we solve the Helmholtz equation for the 3D prism with the combined Neumann and Dirichlet boundary conditions. The Helmholtz equation for the 3D prism with a non-smooth solution is considered in Sect. 3.4. In Sect. 3.5, the screened Poisson equation for the 3D prism with the exact solution given by Eq. (30) is solved. All boundary conditions for the problems in Sects. 3.1–3.3, 3.5 are calculated according to the exact solutions, Eqs. (28)–(30).

3.1 The Helmholtz equation for a cubic domain

Here, we solve a test problem with the exact solution given by Eq. (29) on a regular cubic domain of dimensions

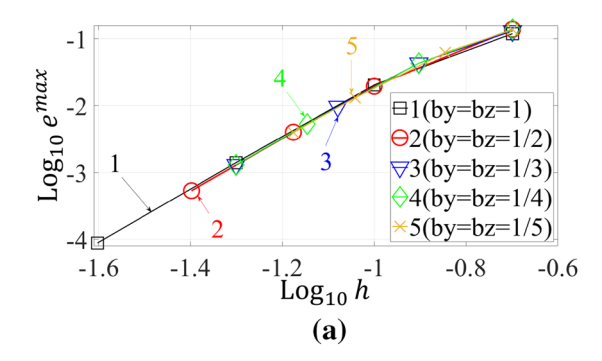
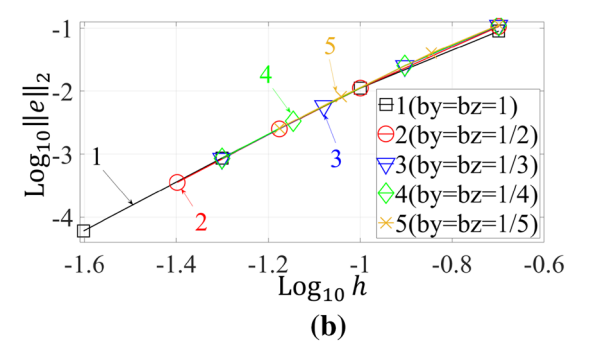


Fig. 3 The maximum relative error e^{\max} (a) and the relative error $\|e\|_2$ (b) as a function of the mesh size h at mesh refinement in the logarithmic scale. The numerical solutions of the 3D Helmholtz equation for the cubic domain with non-zero loading functions and

 $1 \times 1 \times 1$ by OLTEM and conventional linear and high-order finite elements. First, we solved the problem with the Dirichlet boundary conditions along the entire boundary. Then, we solve the same problem with the combined Dirichlet and Neumann boundary conditions given as follows: the Neumann boundary conditions are imposed on face z = 1 and the Dirichlet boundary conditions are imposed along the remaining boundaries; i.e., along the faces x = 0, y = 0, z = 0, x = 1 and y = 1.

To show the effect of the aspect ratios of Cartesian meshes on the accuracy of OLTEM, Fig. 3 presents the maximum relative error e^{\max} and the relative error $\|e\|_2$ on cubic $(b_y = b_z = 1$ —curve 1) and rectangular $(b_y = b_z = 1/2$ —curve 2, $b_y = b_z = 1/3$ —curve 3, $b_y = b_z = 1/4$ —curve 4, $b_y = b_z = 1/5$ —curve 5) Cartesian meshes at mesh refinement. As can be seen from Fig. 3, the mesh refinement in the y- and z-directions practically does not affect the accuracy but increases the number of degrees of freedom. Therefore, in all numerical examples considered below we use cubic $(b_y = b_z = 1)$ Cartesian meshes (the first two terms in the nominator in Eq. (13) for the local truncation error become zero in this case).

To compare the numerical solutions obtained by different techniques the maximum relative error e^{\max} and the relative error $\|e\|_2$ are plotted as a function of the mesh size h in Fig. 4 (the same uniform Cartesian meshes are used for OLTEM and FEM). As can be seen from Fig. 4, OLTEM yields more accurate numerical solutions than those obtained by linear and high-order (up to the fifth order) finite elements at the same mesh size. We should mention that for the fourth and fifth-order elements this is valid for a large range of accuracy up to 0.01% or $\log_{10}e^{\max} = -4$ (for the higher accuracy, the fourth- and fifth-order elements can be more accurate than OLTEM; see Fig. 4). It can also be seen that the order of accuracy of the numerical solution obtained by OLTEM is close to four for the Dirichlet boundary conditions and close to three for the Neumann boundary



the Dirichlet boundary conditions are obtained by OLTEM on cubic $(b_y=b_z=1$ —curve 1) and rectangular $(b_y=b_z=1/2$ —curve 2, $b_y=b_z=1/3$ —curve 3, $b_y=b_z=1/4$ —curve 4, $b_y=b_z=1/5$ —curve 5) Cartesian meshes



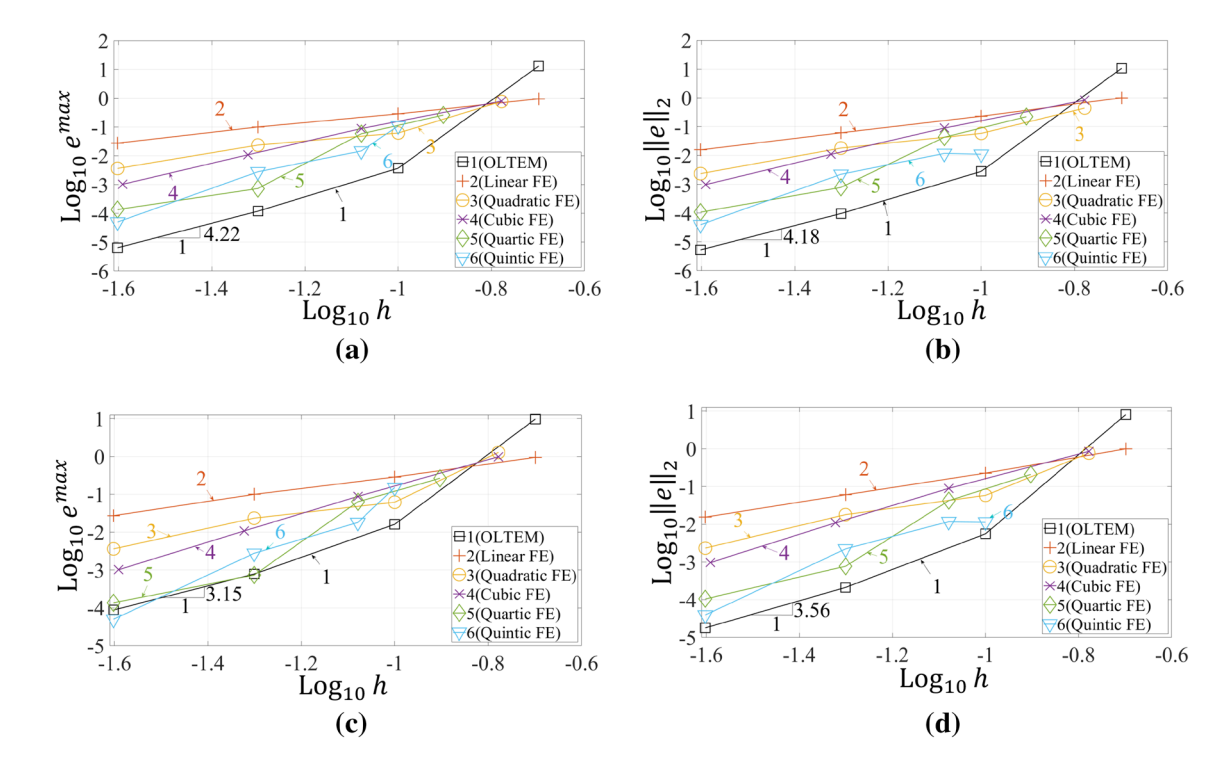


Fig. 4 The maximum relative error e^{\max} (**a**, **c**) and the relative error $\|e\|_2$ (**b**, **d**) as a function of the mesh size h at mesh refinement in the logarithmic scale. The numerical solutions of the 3D Helmholtz equation for the cubic domain with non-zero loading functions and the Dirichlet (**a**, **b**) as well as combined Neumann and Dirichlet (**c**, **d**)

boundary conditions are obtained by OLTEM (curve 1) and by conventional linear and high-order finite elements (curves 2–6) on cubic ($b_y = b_z = 1$) Cartesian meshes. The slopes of curves 2–6 are: 1.88, 2.69, 3.40, 2.44, 5.75 in **a**; 1.97, 2.95, 3.49, 2.86, 5.80 in **b**; 1.87, 2.69, 3.40, 2.43, 5.79 in **c**; and 1.96, 2.94, 3.50, 2.87, 5.82 in **d**

conditions; see the slopes of curves 1 in Fig. 4a, c for the Dirichlet boundary conditions and in Fig. 4b, d for the Neumann boundary conditions. This is in agreement with the theoretical results in Sect. 2.3.

Remark 11 The global matrices of the discrete equations for linear finite elements and for OLTEM on the same Cartesian mesh have the same structure (the same number and positions of zero and nonzero coefficients in the global matrices); the only difference between OLTEM and linear finite elements in this case is in the values of the nonzero coefficients of the global matrices.

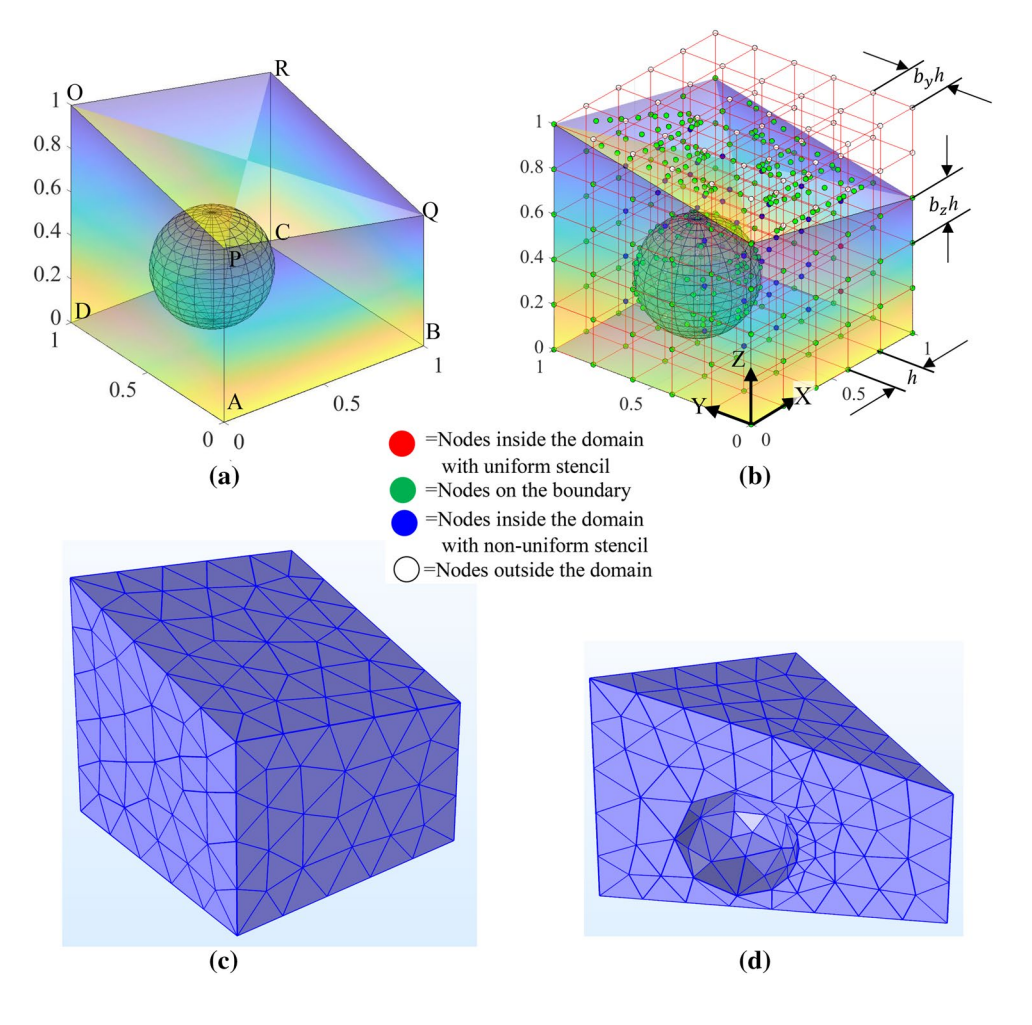
3.2 The Helmholtz equation for the 3D prism with the Dirichlet boundary conditions

Two test problems for the 3D prism with a spherical hole (see Fig. 5a) and the Dirichlet boundary conditions along the entire boundary are solved by OLTEM and by conventional FEM. The exact solutions for these problems are given by Eqs. (28) and (29). The distribution of the exact solution given by Eq. (28) with a lot of local minima and maxima is also shown in Fig. 6a. Figure 6b, c shows the distribution of the relative error on the x = 0.6 and y = 0.4 planes for the numerical solution obtained by OLTEM on the

cubic Cartesian mesh of size h = 1/20. It can be seen that the maximum error occurs inside the domain and far from the boundaries. To compare the accuracy of the numerical solutions obtained by different numerical techniques, Fig. 7 shows the maximum relative error e^{\max} and the relative error $||e||_2$ as a function of the number N of degrees of freedom in the logarithmic scale. As can be seen from Fig. 7, at the same N the numerical results obtained by OLTEM are much more accurate than those obtained by linear and high-order (up to the fifth order) finite elements. We should mention that for the fourth- and fifth-order elements this is valid for a large range of accuracy up to 0.01% or $Log_{10}e^{max} = -4$ (for the higher accuracy the fourth- and fifth-order elements can be more accurate than OLTEM; see Fig. 7). This increase in accuracy is impressive considering the fact that high-order finite elements have much wider stencils compared to those for OLTEM (the width of the stencils used in OLTEM corresponds to that for conventional linear quadrilateral finite elements). Therefore, at a given accuracy OLTEM requires a significantly less computation time compared to that for conventional finite elements. For example, at accuracy of 0.1%, OLTEM reduces the number of degrees of freedom by a factor of greater than 1000 compared to that for linear finite elements with similar stencils; see curves 1 and 2 in Fig. 7 at $Log_{10}e^{max} = -2$. This leads to a huge decrease in



Fig. 5 a A 3D prism ABC-DOPQR (A(0, 0, 0), B(1, 0, 0), C(1, 1, 0), D(0, 1, 0), O(0, 1, 1), P(0, 0, 0.8), Q(1, 0, 0.6), R(1, 1, 0.8))) with a spherical hole of radius 0.25 centered at (0.4, 0.6, 0.3), **b** a cubic Cartesian mesh for OLTEM, **c** an example of a tetrahedral finite element mesh generated by the commercial software COMSOL for the discretization of the prism, **d** shows a part of the mesh in the vicinity of the spherical hole



computational time for OLTEM. The reduction in computational time for OLTEM will be even greater if a higher accuracy is needed.

The order of accuracy of OLTEM is approximately described by the slope of curve 1 at large N in Fig. 7 because the mesh size h is approximately proportional to $\frac{1}{\sqrt[3]{N}}$. As can be seen from Fig. 7 the order of accuracy for the numerical solutions obtained by OLTEM is close to 4. This is in agreement with the theoretical findings in Sect. 2.3 related to OLTEM with the Dirichlet boundary conditions.

It is known that the use of the conventional finite elements with 'cut cells' on Cartesian meshes for irregular domains leads to large condition numbers of the global matrices at mesh refinement and, as a consequence, to inaccurate solutions of the global systems of linear algebraic equations on fine meshes. Figure 8 presents the condition numbers $cn = \frac{|\lambda_{\max}|}{|\lambda_{\min}|}$ of the global matrix of linear algebraic equations for OLTEM on regular (see Sect. 3.1) and irregular (see Fig. 5a) domains as well as for linear finite elements on regular (see Sect. 3.1) domains. Here, λ_{\max} and λ_{\min} are the maximum and minimum eigenvalues of the global

matrix. As can be seen from Fig. 8, at mesh refinement the condition numbers for standard linear finite elements on regular domains grows faster compared to that for OLTEM on irregular domains (see the slopes of the curves 1 and 3 in Fig. 8 where $N^{1/3}$ is proportional to h on Cartesian meshes). This means that at mesh refinement, there are no issues with the condition numbers for OLTEM on irregular domains.

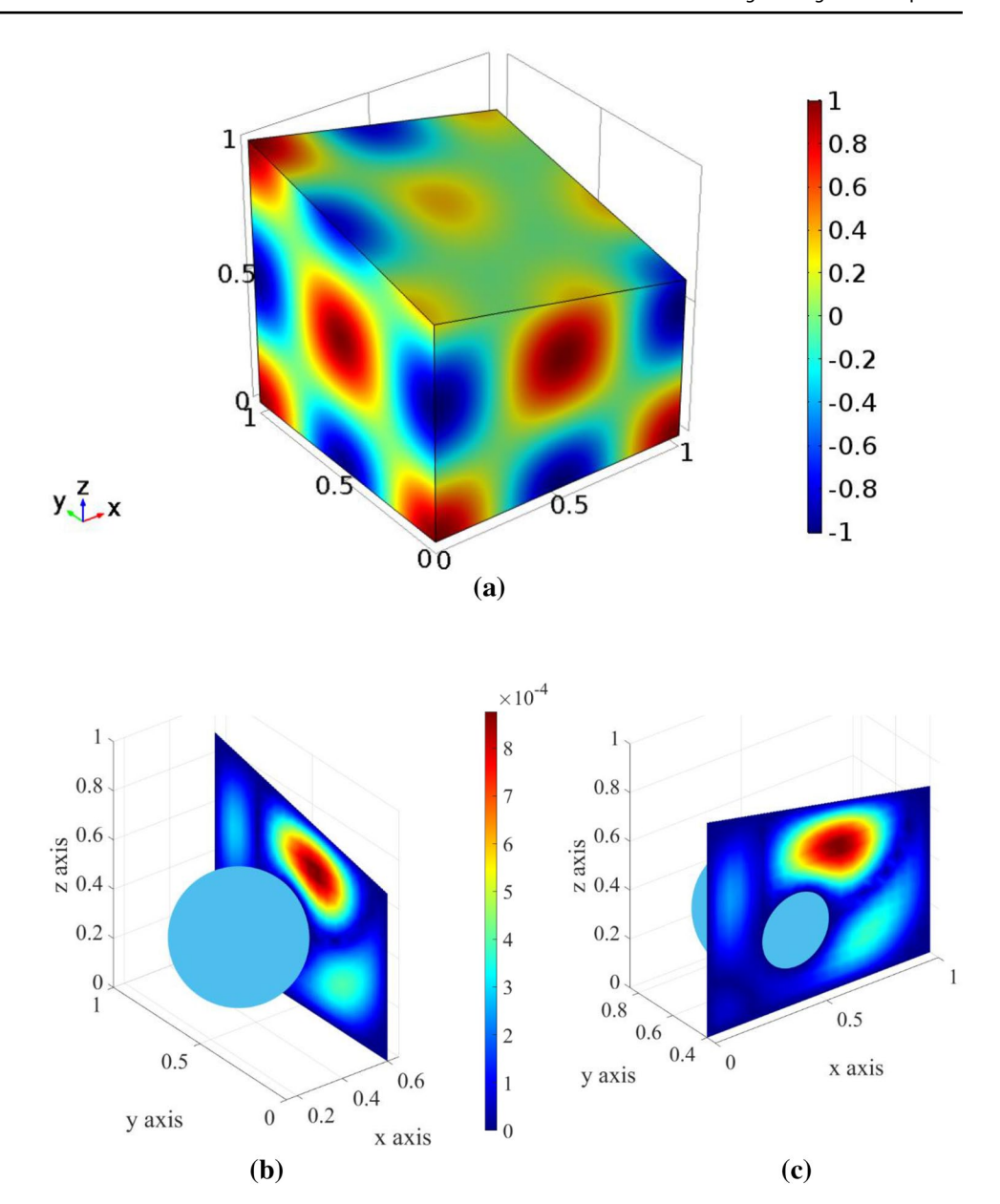
3.3 The Helmholtz equation for the 3D prism with the Neumann boundary conditions

Here, the same test problems for the 3D prism with a spherical hole (see Fig. 5a) as in Sect. 3.2 are solved with the combined Neumann and Dirichlet boundary conditions. The Neumann boundary conditions along the spherical hole and inclined upper boundary face *OPQR* as well as the Dirichlet boundary conditions along rest of the boundary are applied in accordance with the exact solutions Eqs. (28)–(29).

Figure 9 shows the maximum relative error e^{\max} and the relative error $||e||_2$ as a function of the number N of degrees of freedom in the logarithmic scale (similar to Fig. 7). As can be seen from Fig. 9, at the same N the numerical results



Fig. 6 The distribution of the exact solution given by Eq. (28) (a) as well as the distribution of the relative error e (b, c) on the x = 0.4 (b) and y = 0.6 (c) planes obtained by OLTEM on the cubic Cartesian mesh of the mesh size h = 1/20



obtained by OLTEM are more accurate than those obtained by linear and high-order (up to the fifth order) finite elements. We should mention that for the fourth- and fifth-order elements this is valid for a large range of accuracy up to 0.1% or $\text{Log}_{10}e^{\text{max}} = -3$ (for the higher accuracy the fourth- and fifth-order elements can be more accurate than OLTEM; see Fig. 9). It can be also seen from Fig. 9 that the order of accuracy for the numerical solutions obtained by OLTEM is close to 3 (the slope of curve 1 at large N in Fig. 9 approximately describes the order of accuracy for OLTEM). This is in agreement with the theoretical findings in Sect. 2.3.2 related to OLTEM with the Neumann boundary conditions.

To study the convergence and stability of the numerical results obtained by OLTEM in more detail, Fig. 10 presents the curves 1 in Figs. 7a and 9a at small changes of the mesh size h (curves 1 and 2 in Fig. 10 correspond to curves 1 in Figs. 7a and 9a, respectively). For this study, we solve the test problems on 2000 Cartesian meshes with the mesh sizes $h_i = h_1 + \frac{(h_2 - h_1)(i-1)}{1999}$ with $h_1 = 1/10$, $h_2 = 1/30$ and $i = 1, 2, \dots, 2000$. As can be seen from Fig. 10, the numerical results obtained by OLTEM show small oscillations in the convergence curve. The amplitude of these oscillations decreases with the decrease in the mesh size h. This oscillatory behavior can be explained by



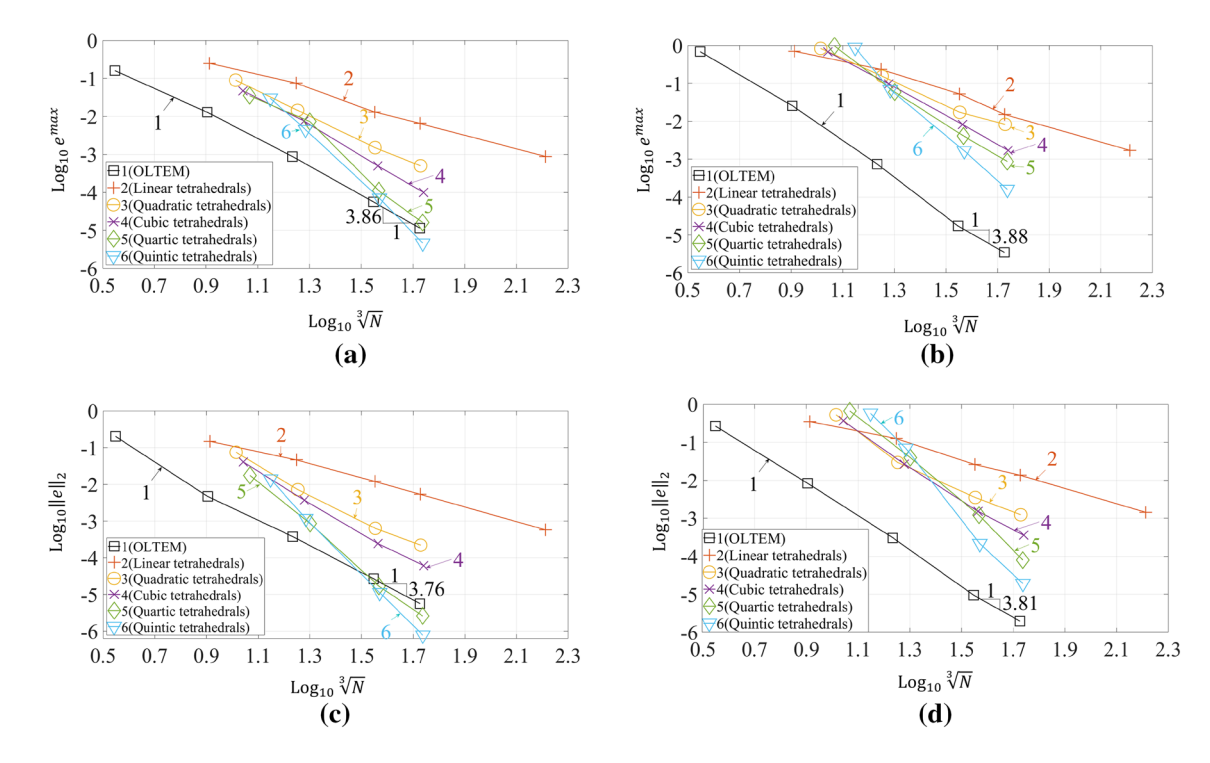


Fig. 7 The maximum relative error e^{\max} (**a**, **b**) and the relative error $\|e\|_2$ (**c**, **d**) as a function of $\sqrt[3]{N}$ at mesh refinement in the logarithmic scale; N is the number of degrees of freedom. The numerical solutions of the 3D Helmholtz equation for the prism (see Fig. 5a) with zero (**a**, **c**), non-zero (**b**, **d**) loading functions and the Dirichlet boundary conditions are obtained by OLTEM on cubic ($b_y = b_z = 1$) Carte-

sian meshes (curve 1) and by conventional linear and high-order finite elements on tetrahedral meshes (curves 2–6). The slopes of curves 2–6 are: 1.78, 2.67, 3.95, 4.93, 7.03 in **a**; 1.95, 1.78, 3.87, 3.57, 6.06 in **b**; 1.99, 2.57, 3.38, 4.67, 6.90 in **c**; and 2.02, 2.62, 3.52,3.33, 6.26 in **d**

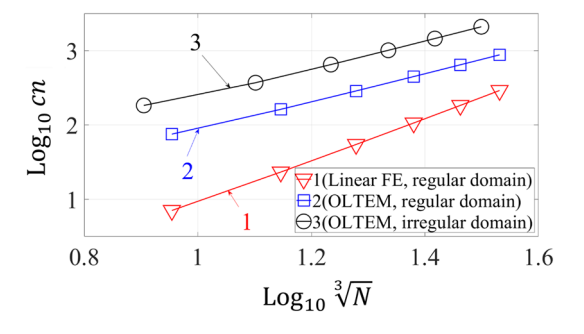


Fig. 8 The condition number cn of the global matrix for OLTEM on regular (curve 2) and irregular (curve 3) domains as well as for linear finite elements on regular (curve 1) domains as a function of $\sqrt[3]{N}$ at mesh refinement in the logarithmic scale; N is the number of degrees of freedom. The slopes of curves 1, 2, 3 are: 2.89, 1.93, 1.94

(1) the complicated dependency of the leading terms of the local truncation error on the coefficients d_i ; and (2) at small changes in the mesh size h, there can be discontinuous changes in the stencil equations due to the change of the location of the nodes. For example, a node located

inside the domain or on the boundary for one mesh can be moved outside the domain for the next mesh. It should be noted that such oscillations in convergence curves are typical for numerical techniques for irregular domain. For instance, the change in the angles of finite elements at small variations of the element size h also leads to such oscillations in the convergence curves for FEM. We should also mention that similar convergence curves for OLTEM have been obtained for the test problem with non-zero loading function considered in this paper.

3.4 The Helmholtz equation for the 3D prism with a non-smooth solution

The Helmholtz equation for the 3D prism with a spherical hole (see Fig. 5), $\beta^2 = 12\pi^2$ and zero loading is considered. The following combined Dirichlet (on faces ABCD, APOD, BCRQ, APQB, CROD and BQRC) and Neumann (along the spherical hole and face PQRO) boundary conditions are applied:



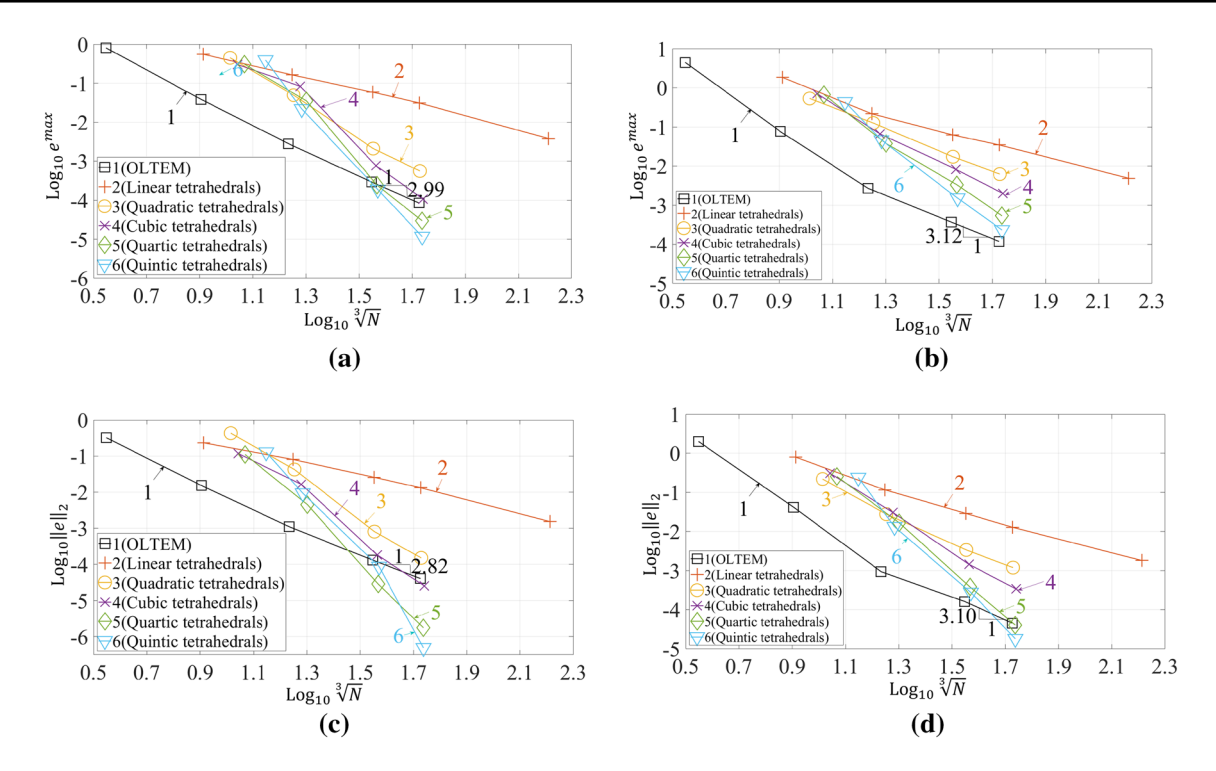


Fig. 9 The maximum relative error e^{\max} (a, b) and the relative error $\|e\|_2$ (c, d) as a function of $\sqrt[3]{N}$ at mesh refinement in the logarithmic scale; N is the number of degrees of freedom. The numerical solutions of the 3D Helmholtz equation for the prism (see Fig. 5a) with zero (a, c), non-zero (b, d) loading functions and the combined Neumann and Dirichlet boundary conditions are obtained by OLTEM on

cubic $(b_y = b_z = 1)$ Cartesian meshes (curve 1) and by conventional linear and high-order finite elements on tetrahedral (curves 2–6) meshes. The slopes of curves 2–6 are: 1.88, 2.50, 4.81, 5.38, 7.17 in a; 1.75, 2.47, 3.50, 4.65, 4.82 in b; 1.93, 2.99, 4.83, 6.00, 13.38 in c; and 1.76, 2.54, 3.56, 4.96, 7.04 in d

On
$$APOD: u(y, z) = \begin{cases} \frac{125}{32}(4y - 1)(4y - 3)(4z - 1)(4z - 3) + \cos(2\pi y)\cos(2\pi z) & \text{inside } EFGH \\ \cos(2\pi y)\cos(2\pi z) & \text{outside } EFGH \end{cases}$$
On $ABCD: u(x, y) = \begin{cases} 49\{(2x - 1)^2 + (2y - 1)^2 - \frac{16}{25}\} + \cos(2\pi x)\cos(2\pi y) & \text{inside circle } M \\ \cos(2\pi x)\cos(2\pi y) & \text{outside circle } M \end{cases}$
On $APQB: u(x, z) = \cos(2\pi x)\cos(2\pi z)$
On $BQRC: u(y, z) = -\cos(2\pi x)\cos(2\pi z)$
On $CDOR: u(x, z) = -\cos(2\pi x)\cos(2\pi z)$
On the spherical hole: $\mathbf{n} \cdot \nabla u = \frac{-2\pi}{\sqrt{(0.4 - x)^2 + (0.6 - y)^2 + (0.3 - z)^2}} \{(0.4 - x)\sin(2\pi x)\cos(2\pi y)\cos(2\pi z) + (0.6 - y)\cos(2\pi x)\sin(2\pi y)\cos(2\pi z) + (0.3 - z)\cos(2\pi x)\cos(2\pi y)\sin(2\pi z)\}$
On $OPQR: \mathbf{n} \cdot \nabla u = \frac{2\pi}{\sqrt{27}} \{\sin(2\pi x)\cos(2\pi y)\cos(2\pi z) - \cos(2\pi x)\sin(2\pi y)\cos(2\pi z) + 5\cos(2\pi x)\cos(2\pi y)\sin(2\pi z)\},$

see also Fig. 11. According to Eq. (31), on faces ABCD and APOD the function u is continuous; however, the boundary conditions on these faces have the discontinuous derivatives along the internal lines that form the internal square EFGH on face APOD (see Fig. 11a) and the internal circle M on face ABCD (see Fig. 11b). For example, on the circle

centered at M on face ABCD: $\frac{\partial u}{\partial x} = 196(2x-1) - 2\pi \sin(2\pi x)\cos(2\pi y)$ inside the circle and $\frac{\partial u}{\partial x} = -2\pi \sin(2\pi x)\cos(2\pi y)$ outside the circle; i.e., along the circle line $(x-0.5)^2 + (y-0.5)^2 = 0.4^2$ these derivatives are discontinuous. Similarly, we have the non-smooth derivatives $\frac{\partial u}{\partial y}$ along the internal circle on the face ABCD as well as the non-smooth derivatives $\frac{\partial u}{\partial x}$ and $\frac{\partial u}{\partial y}$



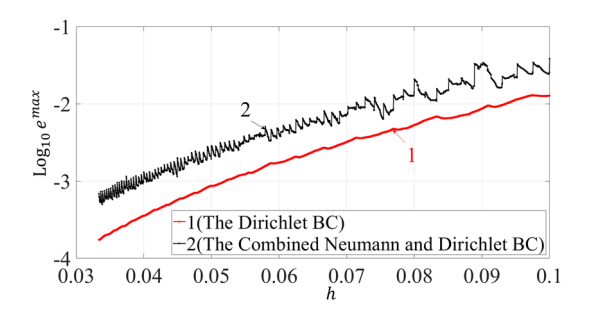
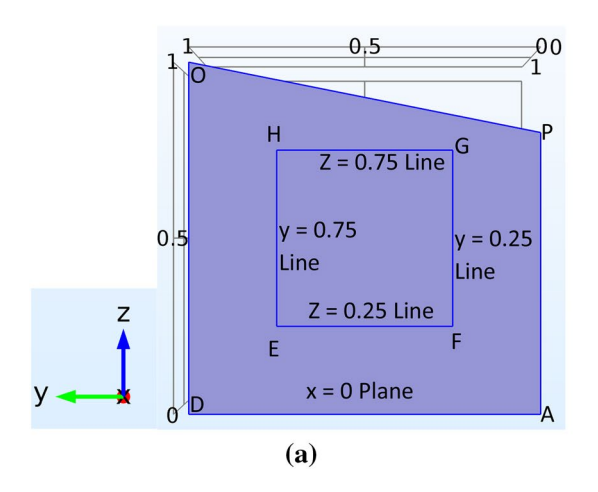


Fig. 10 The logarithm of the maximum relative error e^{\max} as a function of the mesh size h at mesh refinement. The numerical solutions of the 3D Helmholtz equation for the prism (see Fig. 5a) with zero loading function and the Dirichlet boundary conditions (curve 1) as well as the combined Neumann and Dirichlet boundary conditions (curve 2) are obtained by OLTEM on 2000 cubic ($b_y = b_z = 1$) Cartesian meshes with the gradual decrease of the mesh size h (see the text)

along the internal square line *EFGH* on the face *APOD*. For these boundary conditions with the non-smooth derivatives, the exact solution is non-smooth and unknown. Therefore, the numerical solution obtained by the quintic finite elements on a fine mesh with 2,922,089 degrees of freedom is used below as the reference solution.

To compare the accuracy of the numerical solutions obtained by FEM and OLTEM, the problem is solved by OLTEM with unfitted Cartesian meshes and by conventional linear and high-order (up to the fifth order) finite elements on tetrahedral meshes. Figure 12 shows the relative errors e_S at point S(x = 0.1, y = 0.7, z = 0.7) and e_T at point T(x = 0.5, y = 0.1, z = 0.1) as a function of the number N of degrees of freedom in the logarithmic scale. As can be seen from Fig. 12, at the same N the numerical results obtained by OLTEM are much more accurate than those obtained by



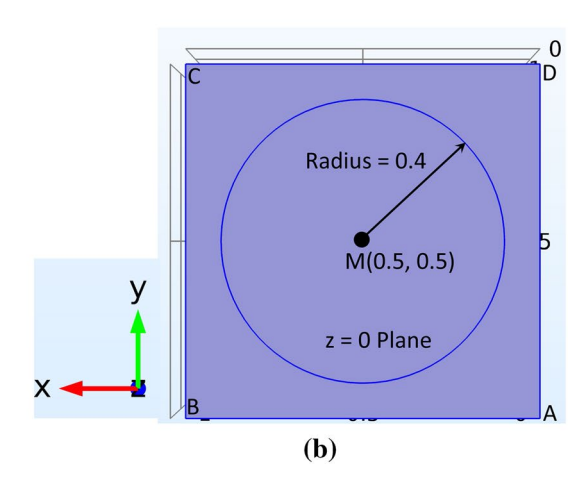
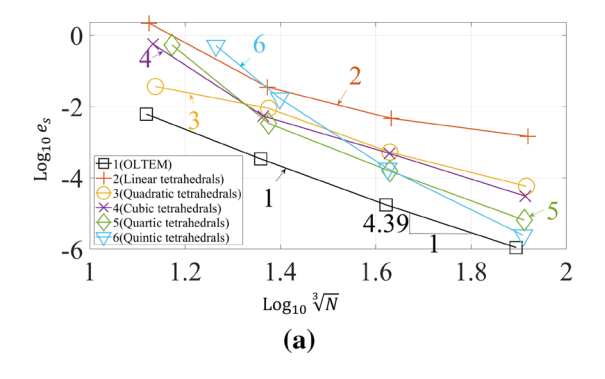


Fig. 11 a The face APOD of the prism (see Fig. 5a) with an internal square EFGH of dimensions 0.5×0.5 . b The face ABCD of the prism (see Fig. 5a) with an internal circle centered at M with the radius of 0.4



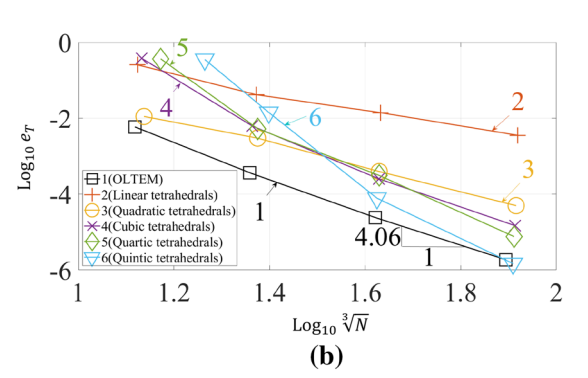


Fig. 12 The relative error e_S at point S(0.1, 0.7, 0.7) (a) and e_T at point T(0.5, 0.1, 0.1) (b) as a function of the number of degrees of freedom N in the logarithmic scale. The numerical solutions of the 3D Helmholtz equation with zero loading function for the prism and the boundary conditions described in Sect. 3.4 are obtained by

OLTEM on square Cartesian meshes (curve 1) and by conventional linear and high-order finite elements on tetrahedral meshes (curves 2–6). The slopes of curves 2–6 are: 1.79, 3.33, 4.20, 5.20, 6.56 in **a**; and 2.07, 3.14, 4.31, 5.15, 6.05 in **b**



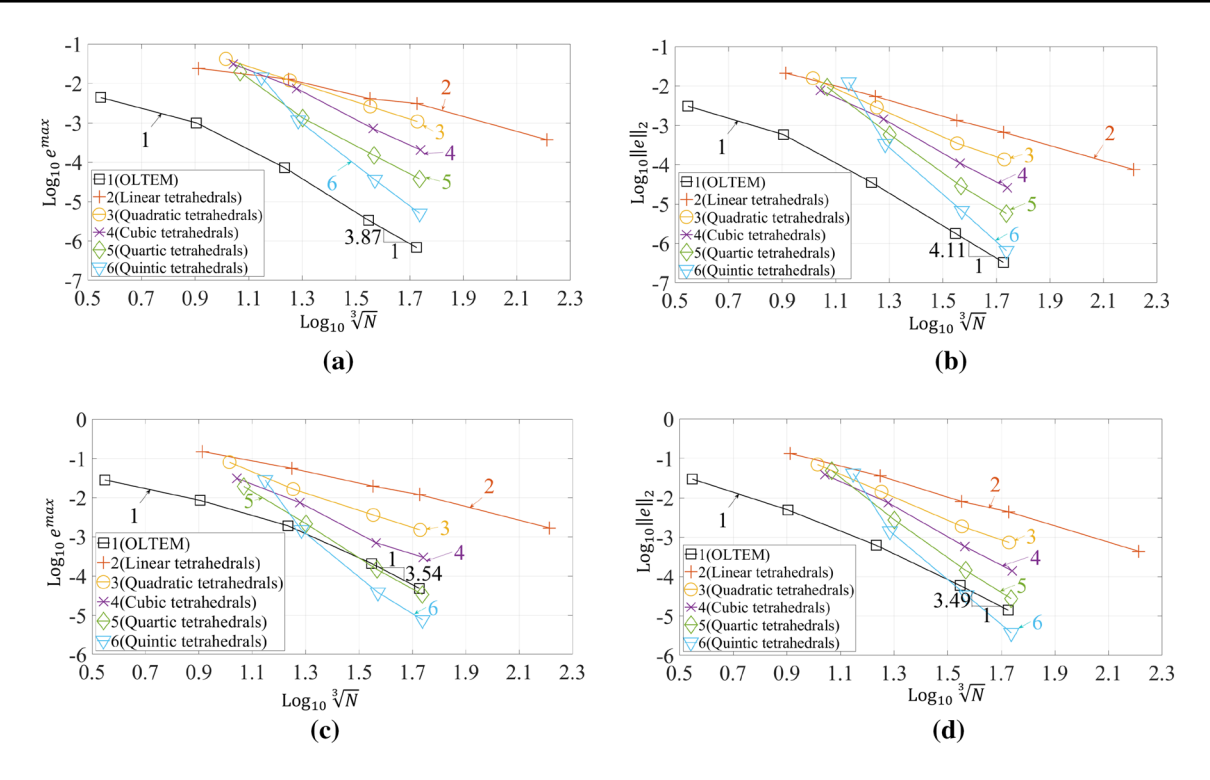


Fig. 13 The maximum relative error e^{\max} (**a**, **c**) and the relative error $\|e\|_2$ (**b**, **d**) as a function of $\sqrt[3]{N}$ at mesh refinement in the logarithmic scale; N is the number of degrees of freedom. The numerical solutions of the 3D screened Poisson equation for the prism (see Fig. 5a) with zero loading function and the Dirichlet (**a**, **b**) as well as com-

bined Neumann and Dirichlet (**c**, **d**) boundary conditions are obtained by OLTEM on cubic ($b_y = b_z = 1$) Cartesian meshes (curve 1) and by conventional linear and high-order (up to the fifth order) finite elements on tetrahedral meshes (curves 2–6)

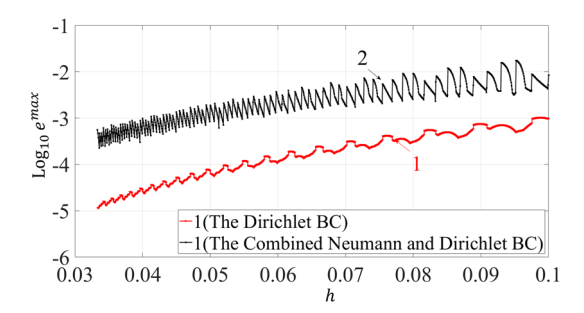


Fig. 14 The logarithm of the maximum relative error e^{\max} as a function of the mesh size h at mesh refinement. The numerical solutions of the 3D screened Poisson equation for the prism (see Fig. 5a) with zero loading function and the Dirichlet boundary conditions (curve 1) as well as the combined Neumann and Dirichlet boundary conditions (curve 2) are obtained by OLTEM on 2000 cubic ($b_y = b_z = 1$) Cartesian meshes with the gradual decrease of the mesh size h (see the text)

linear and high-order (up to the fifth order) finite elements. This is similar to the numerical results obtained in the previous sections. Figure 12 also shows that the order of accuracy of OLTEM for this problem is close four.



First, a test problem for the 3D prism with a spherical hole (see Fig. 5a) for the screened Poisson equation with the Dirichlet boundary conditions along the entire boundary is solved by OLTEM and by FEM. Then, the same test problem for the prism is solved with the combined Neumann and Dirichlet boundary conditions. The Neumann boundary conditions along the spherical hole and inclined upper boundary face *OPQR* as well as the Dirichlet boundary conditions along the remaining boundary are applied. These boundary conditions are evaluated according to the exact solution given by Eq. (30). Figure 13 shows the maximum relative error e^{\max} and the relative error $||e||_2$ as a function of the number N of degrees of freedom in the logarithmic scale. As can be seen from Fig. 13a, at the same N the numerical results obtained by OLTEM are much more accurate than those obtained by linear and high-order (up to the fifth order) finite elements. We should mention that for the fourth and fifth order elements this is valid for a large range of accuracy up to 0.0001% or $Log_{10}e^{max} = -6$ for the Dirichlet boundary conditions (see Fig. 13a,b) and up to 0.1% or $Log_{10}e^{max} = -3$ for the Neumann boundary conditions; see Fig. 13c, d (for



the higher accuracy the fourth- and fifth-order elements can be more accurate than OLTEM; see Fig. 13). It can be also seen from Fig. 13a, b that the order of accuracy for the numerical solutions obtained by OLTEM is close to 4 for the Dirichlet boundary conditions. For the Neumann boundary conditions the order of accuracy for the numerical solutions obtained by OLTEM exceeds 3; see Fig. 13c, d. This is in agreement with the theoretical findings in Sect. 2.3.

To study the convergence and stability of the numerical results obtained by OLTEM in more detail, Fig. 14 presents the curves 1 in Fig. 13a, c at small changes of the mesh size h. Curves 1 and 2 in Fig. 14 correspond to curves 1 in Fig. 13a, c. For this study, we solve the test problem on 2000 Cartesian meshes with the gradual decrease in the mesh sizes (as described in Sect. 3.3). As can be seen from Fig. 14, the numerical results obtained by OLTEM show small oscillations in the convergence curve. The amplitudes of these oscillations decrease with the decrease in the mesh size h at mesh refinement. This oscillatory behavior can be explained similar to that in the previous section.

It can be concluded that for the 3D Helmholtz and screened Poisson equations, OLTEM yields much more accurate results compared to those obtained by linear and high-order (up to the fifth order) finite elements at the same number of degrees of freedom. It is worth to mention that high-order finite elements have much wider stencils and require a greater computational time compared to that for OLTEM.

4 Concluding remarks

Most of the numerical techniques for the solution of partial differential equations finally reduce to a system of discrete or semi-discrete equations. However, in many cases the corresponding stencil equations of these systems do not provide an optimal accuracy. The idea of OLTEM consists in the direct optimization of the coefficients of the stencil equations and it is based on the minimization of the order of the local truncation error. The form and width of the stencil equations in OLTEM are assumed (e.g., as it is assumed for the finite-difference method) or can be selected similar to those for known numerical techniques (in this case, the accuracy of the known numerical techniques can be significantly improved by the modification of the coefficients of the stencil equations). Another idea of OLTEM is the use of simple unfitted Cartesian meshes for complex irregular domain. In the considered paper OLTEM has been applied to the space discretization of the time-independent Helmholtz equation. 27-point stencils in the 3D case that are similar to those for the linear quadrilateral finite elements are considered in the paper. The main advantages of the suggested technique can be summarized as follows:

- The idea of the minimization of the order of the local truncation error of stencil equations can be easily and efficiently applied to the development of new numerical techniques with an optimal accuracy as well as to the accuracy improvement of known numerical methods. Based on this idea, we have developed OLTEM for the 3D Helmholtz equation on irregular domains with Cartesian meshes and simple 27-points stencil equations that provide the optimal accuracy. The main two advantages of the proposed technique are a high optimal accuracy and the use of trivial unfitted Cartesian meshes for irregular domains without the need of complex mesh generators.
- In contrast to many fictitious domain numerical methods, OLTEM uses the exact Dirichlet and Neumann boundary conditions at the actual boundary points without their interpolation using the Cartesian grid points (usually such interpolations introduce additional errors and increase the width of stencils equations for the grid points close to the irregular boundary). The new technique is based on simple 27-point uniform and non-uniform stencils for all internal grid points (inside the domains as well as located close to irregular boundaries).
- In contrast to the finite-difference techniques with the coefficients of the stencils calculated through the approximation of separate partial derivatives, the entire partial differential equation is used for the calculation of the stencil coefficients in OLTEM. This along with the minimization procedure lead to the optimal accuracy of the proposed technique.
- At the same computation costs, OLTEM yields a much higher order of accuracy than other numerical techniques; e.g., than the finite elements. For example, at the similar 27-point stencils, the accuracy of OLTEM is two orders higher than that for the linear finite elements. The numerical results for irregular domains show that at the same number of degrees of freedom and engineering accuracy, OLTEM is even much more accurate than high-order (up to the fifth order!) finite elements with much wider stencils. The numerical results also show that at accuracy of 0.1%, the proposed technique reduces the number of degrees of freedom by a factor of greater than 1000 compared to that for linear finite elements with similar 27-point stencils This leads to a huge decrease in computational time. The reduction in computational time for OLTEM will be even greater if a higher accuracy is needed.
- OLTEM does not require the time consuming numerical integration for finding the coefficients of the stencil equations; e.g., as for high-order finite, spectral and isogeometric elements. For the new technique, the coefficients of the stencil equations for the grid points located far from the boundary are calculated analytically. For



- the grid points located close to the boundary (with nonuniform and cut stencils), the coefficients of the stencil equations are calculated numerically by the solution of small local systems of linear algebraic equations.
- In our papers [65, 66], we have developed OLTEM for the 3D wave, heat and Poisson equations. Despite the same idea, the stencils, derivations and the imposition of the Neumann boundary conditions for the time-independent 3D Poisson equation (see [65, 66]) and the Helmholtz equation (the current paper) are different. E.g., we use 27 stencil coefficients, minimize 45 b, coefficients in the local truncation error (including up to the sixth-order terms with respect to h) for the Poisson equations while we use 54 stencil coefficients, minimize 165 b; coefficients in the local truncation error (including up to the eighth-order terms with respect to h) for the Helmholtz equation. For the same Neumann boundary conditions, we use twice the number of stencil coefficients for the Helmholtz equation compared to that for the Poisson equation.
- It has been shown that the Helmholtz and screened Poisson equations can be uniformly treated with OLTEM.

In the future, we plan to consider the stencils with a larger numbers of grid points for a higher order of accuracy (similar to the high-order finite elements or to the high-order finite-difference techniques), to consider a mesh refinement with Cartesian meshes using special stencils for the transition from a fine mesh to a coarse mesh, to consider other boundary conditions (e.g., the Robin conditions), to solve real-world problems with OLTEM. We also plan to study the application of OLTEM to more complicated scalar PDEs and systems of PDEs that include mixed derivatives and higher-order derivatives. For example, in [73, 74] we successfully applied OLTEM on regular domains to a system of 2D elasticity equations that include two PDEs with mixed derivatives.

Appendix 1: The coefficients b_p used in Eq. (10) in Sect. 2.2

The first five coefficients b_p ($p=1,2,\ldots,5$) used in Eq. (10) are presented below. All coefficients b_p used in Eq. (10) are given in the attached files 'b-coeff-1.pdf' and 'b-coeff-1.nb'. Eq. (10):

$$\begin{split} b_1 = & k_1 + k_{10} + k_{11} + k_{12} + k_{13} + k_{14} + k_{15} + k_{16} \\ & + k_{17} + k_{18} + k_{19} + k_2 + k_{20} + k_{21} + k_{22} + k_{23} \\ & + k_{24} + k_{25} + k_{26} + k_{27} + k_3 + k_4 + k_5 + k_6 + k_7 + k_8 + k_9 \\ b_2 = & - d_1k_1 - d_{10}k_{10} + d_{12}k_{12} - d_{13}k_{13} \\ & + d_{15}k_{15} - d_{16}k_{16} + d_{18}k_{18} - d_{19}k_{19} + d_{21}k_{21} - d_{22}k_{22} + d_{24}k_{24} \\ & - d_{25}k_{25} + d_{27}k_{27} + d_3k_3 - d_4k_4 + d_6k_6 - d_7k_7 + d_9k_9 \\ b_3 = & b_y(-d_1k_1 - d_{10}k_{10} - d_{11}k_{11} - d_{12}k_{12} \\ & + d_{16}k_{16} + d_{17}k_{17} + d_{18}k_{18} - d_{19}k_{19} - d_2k_2 \\ & - d_{20}k_{20} - d_{21}k_{21} + d_{25}k_{25} + d_{26}k_{26} + d_{27}k_{27} \\ & - d_3k_3 + d_7k_7 + d_8k_8 + d_9k_9) \\ b_4 = & b_z(-d_1k_1 + d_{19}k_{19} - d_2k_2 + d_{20}k_{20} \\ & + d_{21}k_{21} + d_{22}k_{22} + d_{23}k_{23} + d_{24}k_{24} + d_{25}k_{25} + d_{26}k_{26} \\ & + d_{27}k_{27} - d_3k_3 - d_4k_4 - d_5k_5 - d_6k_6 \\ & - d_7k_7 - d_8k_8 - d_9k_9) \\ b_5 = & b_y(d_1^2k_1 + d_{10}^2k_{10} - d_{12}^2k_{12} - d_{16}^2k_{16} \\ & + d_{18}^2k_{18} + d_{19}^2k_{19} - d_{21}^2k_{21} - d_{25}^2k_{25} \\ & + d_{27}k_{27} - d_3^2k_3 - d_7^2k_7 + d_9^2k_9). \end{split}$$

Appendix 2: The coefficients b_p used in Eq. (10) for the Neumann boundary conditions in Sect. 2.3

The first five coefficients b_p ($p=1,2,\ldots,5$) used in Eq. (10) are presented below. All coefficients b_p used in Eq. (10) are given in the attached files 'b-coeff-2.pdf' and 'b-coeff-2.nb'. Equation (10):



$$\begin{array}{l} b_1 = & k_1 + k_{10} + k_{11} + k_{12} + k_{13} + k_{14} + k_{15} + k_{16} + k_{17} + k_{18} + k_{19} + k_2 + k_{20} \\ & + k_{21} + k_{22} + k_{23} + k_{24} + k_{25} + k_{26} + k_{27} + k_{3} + k_{4} + k_{5} + k_{6} + k_{7} + k_{8} + k_{9} \\ b_2 = & -d_1k_1 - d_{10}k_{10} + d_{12}k_{12} - d_{12}k_{13} + d_{15}k_{15} - d_{16}k_{16} + d_{18}k_{18} - d_{19}k_{19} \\ & + d_{21}k_{21} - d_{22}k_{22} + d_{24}k_{24} - d_{25}k_{25} + d_{27}k_{27} + d_{3}k_{3} - d_{4}k_{4} + d_{6}k_{6} - d_{7}k_{7} \\ & + d_{9}k_{9} + \bar{k}_{1}n_{1,1} + \bar{k}_{10}n_{1,10} + \bar{k}_{11}n_{1,11} + \bar{k}_{12}n_{1,12} + \bar{k}_{13}n_{1,13} + \bar{k}_{14}n_{1,14} + \bar{k}_{15}n_{1,15} \\ & + \bar{k}_{16}n_{1,16} + \bar{k}_{17}n_{1,17} + \bar{k}_{18}n_{1,18} + \bar{k}_{19}n_{1,19} + \bar{k}_{2}n_{1,2} + \bar{k}_{20}n_{1,20} + \bar{k}_{21}n_{1,21} \\ & + \bar{k}_{22}n_{1,22} + \bar{k}_{23}n_{1,23} + \bar{k}_{24}n_{1,24} + \bar{k}_{25}n_{1,25} + \bar{k}_{26}n_{1,26} + \bar{k}_{27}n_{1,27} + \bar{k}_{3}n_{1,3} + \bar{k}_{4}n_{1,4} \\ & + \bar{k}_{3}n_{1,5} + \bar{k}_{6}n_{1,6} + \bar{k}_{7}n_{1,7} + \bar{k}_{8}n_{1,8} + \bar{k}_{9}n_{1,9} \\ b_3 = b_3(-d_1k_1 - d_10k_{10} - d_{11}k_{11} - d_{12}k_{12} + d_{16}k_{16} + d_{17}k_{17} + d_{18}k_{18} - d_{19}k_{19} - d_{2}k_{2} \\ & - d_{20}k_{20} - d_{21}k_{21} + d_{25}k_{25} + d_{26}k_{26} + d_{27}k_{27} - d_{3}k_{3} + d_{7}k_{7} + d_{8}k_{8} + d_{9}k_{9}) \\ & + \bar{k}_{1}n_{2,1} + \bar{k}_{10}n_{2,10} + \bar{k}_{11}n_{2,11} + \bar{k}_{12}n_{2,12} + \bar{k}_{13}n_{2,13} + \bar{k}_{14}n_{2,14} + \bar{k}_{15}n_{2,15} \\ & + \bar{k}_{16}n_{2,16} + \bar{k}_{17}n_{2,17} + \bar{k}_{18}n_{2,18} + \bar{k}_{19}n_{2,19} + \bar{k}_{2}n_{2,27} + \bar{k}_{3}n_{2,3} + \bar{k}_{4}n_{2,4} \\ & + \bar{k}_{3}n_{2,23} + \bar{k}_{24}n_{2,24} + \bar{k}_{25}n_{2,25} + \bar{k}_{26}n_{2,6} + \bar{k}_{27}n_{2,27} + \bar{k}_{3}n_{3,3} + \bar{k}_{4}n_{3,4} \\ & + d_{25}k_{25} + d_{26}k_{26} + d_{27}k_{27} - d_{3}k_{3} - d_{4}k_{4} - d_{5}k_{5} - d_{6}k_{6} - d_{7}k_{7} - d_{8}k_{8} - d_{9}k_{9}) \\ & + \bar{k}_{1}n_{3,1} + \bar{k}_{19}n_{3,19} + \bar{k}_{2}n_{3,2} + \bar{k}_{20}n_{3,2} + \bar{k}_{20}n_{3,2} + \bar{k}_{20}n_{3,2} \\ & + \bar{k}_{23}n_{3,23} + \bar{k}_{24}n_{3,24} + \bar{k$$



Acknowledgements The research has been supported in part by the NSF Grant CMMI-1935452 and by Texas Tech University.

References

- Kacimi AE, Laghrouche O, Mohamed M, Trevelyan J (2019) Bernstein-Bézier based finite elements for efficient solution of short wave problems. Comput Methods Appl Mech Eng 343:166-185
- Lieu A, Gabard G, Bériot H (2016) A comparison of high-order polynomial and wave-based methods for Helmholtz problems. J Comput Phys 321:105–125
- Celiker E, Lin P (2019) A highly-accurate finite element method with exponentially compressed meshes for the solution of the Dirichlet problem of the generalized Helmholtz equation with corner singularities. J Comput Appl Math 361:227–235
- Magoulès F, Zhang H (2018) Three-dimensional dispersion analysis and stabilized finite element methods for acoustics. Comput Methods Appl Mech Eng 335:563–583
- Lam CY, Shu C-W (2017) A phase-based interior penalty discontinuous Galerkin method for the Helmholtz equation with spatially varying wavenumber. Comput Methods Appl Mech Eng 318:456–473
- Diwan GC, Mohamed MS (2019) Pollution studies for high order isogeometric analysis and finite element for acoustic problems. Comput Methods Appl Mech Eng 350:701–718
- Harari I (2006) A survey of finite element methods for timeharmonic acoustics. Comput Methods Appl Mech Eng 195(13):1594–1607
- 8. Babuška I, Ihlenburg F, Paik ET, Sauter SA (1995) A generalized finite element method for solving the Helmholtz equation in two dimensions with minimal pollution. Comput Methods Appl Mech Eng 128(3):325–359
- Biermann J, von Estorff O, Petersen S, Wenterodt C (2009) Higher order finite and infinite elements for the solution of Helmholtz problems. Comput Methods Appl Mech Eng 198(13):1171-1188
- Fang J, Qian J, Zepeda-Núñez L, Zhao H (2018) A hybrid approach to solve the high-frequency Helmholtz equation with source singularity in smooth heterogeneous media. J Comput Phys 371:261–279
- Christodoulou K, Laghrouche O, Mohamed M, Trevelyan J (2017) High-order finite elements for the solution of Helmholtz problems. Comput Struct 191:129–139
- Gerdes K, Ihlenburg F (1999) On the pollution effect in FE solutions of the 3D-Helmholtz equation. Comput Methods Appl Mech Eng 170(1):155–172
- Demkowicz L, Gopalakrishnan J, Muga I, Zitelli J (2012) Wavenumber explicit analysis of a DPG method for the multidimensional Helmholtz equation. Comput Methods Appl Mech Eng 213–216:126–138
- Mascotto L, Perugia I, Pichler A (2019) A nonconforming Trefftz virtual element method for the Helmholtz problem: numerical aspects. Comput Methods Appl Mech Eng 347:445–476
- Yang M, Perrey-Debain E, Nennig B, Chazot J-D (2018) Development of 3D PUFEM with linear tetrahedral elements for the simulation of acoustic waves in enclosed cavities. Comput Methods Appl Mech Eng 335:403–418
- Eslaminia M, Guddati MN (2016) A double-sweeping preconditioner for the Helmholtz equation. J Comput Phys 314:800–823

- Amara M, Calandra H, Dejllouli R, Grigoroscuta-Strugaru M
 (2012) A stable discontinuous Galerkin-type method for solving efficiently Helmholtz problems. Comput Struct 106–107:258–272
- Banerjee S, Sukumar N (2017) Exact integration scheme for planewave-enriched partition of unity finite element method to solve the Helmholtz problem. Comput Methods Appl Mech Eng 317:619–648
- Strouboulis T, Babuška I, Hidajat R (2006) The generalized finite element method for Helmholtz equation: theory, computation, and open problems. Comput Methods Appl Mech Eng 195(37):4711–4731
- Chaumont-Frelet T (2016) On high order methods for the heterogeneous Helmholtz equation. Comput Math Appl 72(9):2203–2225
- He Z, Liu G, Zhong Z, Wu S, Zhang G, Cheng A (2009) An edge-based smoothed finite element method (ES-FEM) for analyzing three-dimensional acoustic problems. Comput Methods Appl Mech Eng 199(1):20–33
- Wu Z, Alkhalifah T (2018) A highly accurate finite-difference method with minimum dispersion error for solving the Helmholtz equation. J Comput Phys 365:350–361
- You X, Chai Y, Li W (2019) A coupled FE-meshfree method for Helmholtz problems using point interpolation shape functions and edge-based gradient smoothing technique. Comput Struct 213:1–22
- Coox L, Deckers E, Vandepitte D, Desmet W (2016) A performance study of NURBS-based isogeometric analysis for interior two-dimensional time-harmonic acoustics. Comput Methods Appl Mech Eng 305:441

 –467
- Dinachandra M, Raju S (2018) Plane wave enriched partition of unity isogeometric analysis (PUIGA) for 2D-Helmholtz problems. Comput Methods Appl Mech Eng 335:380–402
- Khajah T, Villamizar V (2019) Highly accurate acoustic scattering: isogeometric analysis coupled with local high order farfield expansion ABC. Comput Methods Appl Mech Eng 349:477–498
- Galagusz R, McFee S (2019) An iterative domain decomposition, spectral finite element method on non-conforming meshes suitable for high frequency Helmholtz problems. J Comput Phys 379:132–172
- Gordon D, Gordon R, Turkel E (2015) Compact high order schemes with gradient-direction derivatives for absorbing boundary conditions. J Comput Phys 297:295–315
- Cheng D, Liu Z, Wu T (2015) A multigrid-based preconditioned solver for the Helmholtz equation with a discretization by 25-point difference scheme. Math Comput Simul 117:54–67
- 30. Turkel E, Gordon D, Gordon R, Tsynkov S (2013) Compact 2D and 3D sixth order schemes for the Helmholtz equation with variable wave number. J Comput Phys 232(1):272–287
- Britt S, Tsynkov S, Turkel E (2018) Numerical solution of the wave equation with variable wave speed on nonconforming domains by high-order difference potentials. J Comput Phys 354:26–42
- Jones TN, Sheng Q (2019) Asymptotic stability of a dual-scale compact method for approximating highly oscillatory Helmholtz solutions. J Comput Phys 392:403

 –418
- Wu T (2017) A dispersion minimizing compact finite difference scheme for the 2D Helmholtz equation. J Comput Appl Math 311:497–512
- Wu T, Xu R (2018) An optimal compact sixth-order finite difference scheme for the Helmholtz equation. Comput Math Appl 75(7):2520–2537
- Stolk CC (2016) A dispersion minimizing scheme for the 3-D Helmholtz equation based on ray theory. J Comput Phys 314:618–646
- 36. Vos P, van Loon R, Sherwin S (2008) A comparison of fictitious domain methods appropriate for spectral/hp



- element discretisations. Comput Methods Appl Mech Eng 197(25-28):2275-2289
- Burman E, Hansbo P (2010) Fictitious domain finite element methods using cut elements: I. A stabilized Lagrange multiplier method. Comput Methods Appl Mech Eng 199(41–44):2680–2686
- Rank E, Ruess M, Kollmannsberger S, Schillinger D, Duster A (2012) Geometric modeling, isogeometric analysis and the finite cell method. Comput Methods Appl Mech Eng 249–252:104–115
- Fries T, Omerović S, Schöllhammer D, Steidl J (2017) Higherorder meshing of implicit geometries-part I: integration and interpolation in cut elements. Comput Methods Appl Mech Eng 313:759–784
- Hoang T, Verhoosel CV, Auricchio F, van Brummelen EH, Reali A (2017) Mixed isogeometric finite cell methods for the Stokes problem. Comput Methods Appl Mech Eng 316:400–423
- 41. May S, Berger M (2017) An explicit implicit scheme for cut cells in embedded boundary meshes. J Sci Comput 71(3):919–943
- Kreisst H-O, Petersson NA (2006) An embedded boundary method for the wave equation with discontinuous coefficients. SIAM J Sci Comput 28(6):2054–2074
- Kreiss H-O, Petersson NA (2006) A second order accurate embedded boundary method for the wave equation with Dirichlet data. SIAM J Sci Comput 27(4):1141–1167
- 44. Jomaa Z, Macaskill C (2010) The Shortley–Weller embedded finite-difference method for the 3D Poisson equation with mixed boundary conditions. J Comput Phys 229(10):3675–3690
- Jomaa Z, Macaskill C (2005) The embedded finite difference method for the Poisson equation in a domain with an irregular boundary and Dirichlet boundary conditions. J Comput Phys 202(2):488–506
- Hellrung JL Jr, Wang L, Sifakis E, Teran JM (2012) A second order virtual node method for elliptic problems with interfaces and irregular domains in three dimensions. J Comput Phys 231(4):2015–2048
- Chen L, Wei H, Wen M (2017) An interface-fitted mesh generator and virtual element methods for elliptic interface problems. J Comput Phys 334:327–348
- Bedrossian J, von Brecht JH, Zhu S, Sifakis E, Teran JM (2010) A second order virtual node method for elliptic problems with interfaces and irregular domains. J Comput Phys 229(18):6405–6426
- Mattsson K, Almquist M (2017) A high-order accurate embedded boundary method for first order hyperbolic equations. J Comput Phys 334:255–279
- Schwartz P, Barad M, Colella P, Ligocki T (2006) A Cartesian grid embedded boundary method for the heat equation and Poisson's equation in three dimensions. J Comput Phys 211(2):531–550
- Colella P, Graves DT, Keen BJ, Modiano D (2006) A Cartesian grid embedded boundary method for hyperbolic conservation laws. J Comput Phys 211(1):347–366
- Crockett R, Colella P, Graves D (2011) A Cartesian grid embedded boundary method for solving the Poisson and heat equations with discontinuous coefficients in three dimensions. J Comput Phys 230(7):2451–2469
- McCorquodale P, Colella P, Johansen H (2001) A Cartesian grid embedded boundary method for the heat equation on irregular domains. J Comput Phys 173(2):620–635
- Angel JB, Banks JW, Henshaw WD (2018) High-order upwind schemes for the wave equation on overlapping grids: Maxwell's equations in second-order form. J Comput Phys 352:534–567
- Uddin H, Kramer R, Pantano C (2014) A Cartesian-based embedded geometry technique with adaptive high-order finite differences for compressible flow around complex geometries. J Comput Phys 262:379

 –407
- Main A, Scovazzi G (2018) The shifted boundary method for embedded domain computations. Part I: Poisson and Stokes problems. J Comput Phys 372:972–995

- Song T, Main A, Scovazzi G, Ricchiuto M (2018) The shifted boundary method for hyperbolic systems: embedded domain computations of linear waves and shallow water flows. J Comput Phys 369:45–79
- Hosseinverdi S, Fasel HF (2018) An efficient, high-order method for solving Poisson equation for immersed boundaries: combination of compact difference and multiscale multigrid methods. J Comput Phys 374:912–940
- Huang J, Bathe K-J (2019) Quadrilateral overlapping elements and their use in the amore paradigm. Comput Struct 222:25–35
- Rank E, Kollmannsberger S, Sorger C, Duster A (2011) Shell finite cell method: a high order fictitious domain approach for thin-walled structures. Comput Methods Appl Mech Eng 200(45–46):3200–3209
- Kreiss H-O, Petersson NA, Ystrom J (2004) Difference approximations of the Neumann problem for the second order wave equation. SIAM J Numer Anal 42(3):1292–1323
- Johansen H, Colella P (1998) A Cartesian grid embedded boundary method for Poisson's equation on irregular domains. J Comput Phys 147(1):60–85
- Medvinsky M, Tsynkov S, Turkel E (2016) Solving the Helmholtz equation for general smooth geometry using simple grids. Wave Motion 62:75–97
- Idesman A, Dey B (2020) A new numerical approach to the solution of the 2-D Helmholtz equation with optimal accuracy on irregular domains and Cartesian meshes. Comput Mech 65:1189–1204
- Idesman A, Dey B (2019) A new 3-D numerical approach to the solution of PDEs with optimal accuracy on irregular domains and Cartesian meshes. Comput Methods Appl Mech Eng 354:568–592
- 66. Idesman A, Dey B (2020) The treatment of the Neumann boundary conditions for a new numerical approach to the solution of PDEs with optimal accuracy on irregular domains and Cartesian meshes. Comput Methods Appl Mech Eng 365:112985
- Singer I, Turkel E (2006) Sixth-order accurate finite difference schemes for the Helmholtz equation. J Comput Acoust 14(03):339–351
- Sutmann G (2007) Compact finite difference schemes of sixth order for the Helmholtz equation. J Comput Appl Math 203(1):15-31
- 69. Idesman A, Dey B (2020) A high-order numerical approach with Cartesian meshes for modeling of wave propagation and heat transfer on irregular domains with inhomogeneous materials. Comput Methods Appl Mech Eng 370:113249
- Idesman A, Dey B (2017) The use of the local truncation error for the increase in accuracy of the linear finite elements for heat transfer problems. Comput Methods Appl Mech Eng 319:52–82
- Bathe KJ (1996) Finite element procedures. Prentice-Hall Inc., Upper Saddle River
- Langtangen HP, Linge S (2017) Finite difference computing with PDEs. Springer, Berlin
- Idesman A, Dey B (2020) Compact high-order stencils with optimal accuracy for numerical solutions of 2-D time-independent elasticity equations. Comput Methods Appl Mech Eng 360:112699
- Idesman A, Dey B (2020) Accurate numerical solutions of 2-D elastodynamics problems using compact high-order stencils. Comput Struct 229:106160

Publisher's Note Springer Nature remains neutral with regard to jurisdictional claims in published maps and institutional affiliations.

